universitätbonn
Rheinische
Friedrich-Wilhelms-
Universität Bonn

Ultrafast Carrier Dynamics and Coherent Phonon Oscillations in PbTe

Masterarbeit in Physik

von

Kiran Horabail Prabhakara

angefertigt im Institut

II. Physikalisches Insitut, University of Cologne

vorgelegt der

Mathematisch-Naturwissenschaftlichen Fakultät

der

Universität Bonn

June 2015

Gutachter 1: Prof.Dr.Ir. H.M.Paul van Loosdrecht

Gutachter 2: Prof.Dr. Dieter Meschede

Declaration of Authorship

I, Kiran Horabail Prabhakara, declare that this thesis titled, ‘Ultrafast Carrier Dynamics and Coherent Phonon Oscillations in PbTe’ and the work presented in it are my own. I confirm that:

- This work was done wholly or mainly while in candidature for a Masters degree at this University.
- Where I have consulted the published work of others, this is always clearly attributed.
- Where I have quoted from the work of others, the source is always given. With the exception of such quotations, this thesis is entirely my own work.
- I have acknowledged all main sources of help.

Signed: ____________________________

Date: ____________________________

Abstract

Thermoelectric materials are at the forefront of the energy revolution. These materials represent one of the best solutions to recover the energy lost in the form of heat. Efficient thermoelectrics require good electrical conductivity and low thermal conductivity. PbTe is an ideal thermoelectric because of it's unusually low thermal conductivity. However the origins are still in question. In this work we use ultrafast white light pump-probe spectroscopy to demonstrate coherent squeezed states involving TO and LA phonons. In addition to that, we also investigate electron-phonon coupling mechanisms, that supports the theory of TO and LA mode softening.

Acknowledgements

I would like to take this opportunity to thank some people who have been substantial in my growth both academic and otherwise. I firstly would like to thank Prof. Dr. Ir. H. M. Paul Van Loosdrecht for giving me the opportunity to work in the optical condensed matter group of the Institute of Theoretical Physics, University of Cologne and providing me with a great working environment. I also thank him for his timely inputs and support in his capacity as first supervisor. I would like to thank Prof. Dieter Meschede for agreeing to be the second evaluator for my Master Thesis. I have to thank my fellow masters students, PhD. students, in our group for their contributions in discussions and helping in making the experiments easier. Many thanks to some of my peers and friends here who have helped me make the thesis more presentable with their suggestions and opinions, in this regard I would like to thank Manpreet Kaur, Smaran Deshmukh, V.K Bharadwaj, Prashant, Bernard, Kestas, Henning and the list keeps growing. I also thank all my friends in Bonn, who have made my stay here enjoyable. I also have to thank all my friends back in India who have inspired me along the way. Last but not least, I would like to extend my thanks to all those great teachers I have had the honour of being a student under, for inspiring me to continue doing science.

Contents

List of Figures

List of Tables

“If you wish to make an apple pie from scratch, you must first invent the universe” - Carl Sagan

Chapter 1

Introduction

Understanding the underlying microscopic mechanisms invloved in ultrafast carrier thermalization and energy relaxation is one of the key factors in improving the speed of information processing systems may lead to faster electronics. For example, a typical transport time of a majority charge carrier from the source terminal to the drain terminal via an applied gate voltage in a field effect transistor is about a picosecond. Thus, understanding the possible scattering mechanisms that could be involved during transport can have a major impact on improving processing speeds. Understanding ultrafast dynamics however is not a semiconductor/-condensed matter specific problem; the study of certain reaction dynamics of chemical processes or even microscopic dynamics of biological systems [28] are also examples of topics that can be addressed using ultrafast techniques. As such, we need a tool to study the dynamical aspects of these ultrafast microscopic processes. This should motivate us towards spectroscopic techniques that can study the material characteristics on a time domain basis.

Time-resolved methods have their origins as early as the 1870's. One of the notable methods involved *time lapse photography*, famously applied to the problem of a trotting horse. The question was whether a trotting horse had all of it's legs in the air at any time during the course of it's motion. This was answered through a series of time lapse shots of the trotting horse which was later stitched together to find out that it indeed had all of it's legs in the air (see figure 1.1) at a particular instance of time! Later, during the 1950's, this method was extended to the study of the time-resolved emission spectrum of an electric discharge using a stroboscopic technique [4]. The idea was to use a rotating slit to photograph the discharge and record this on a photosensitive tape. With the advent of pulsed lasers during the 1980's, time-resolved spectroscopic techniques have evolved to study processes that happen on a femtosecond timescale.

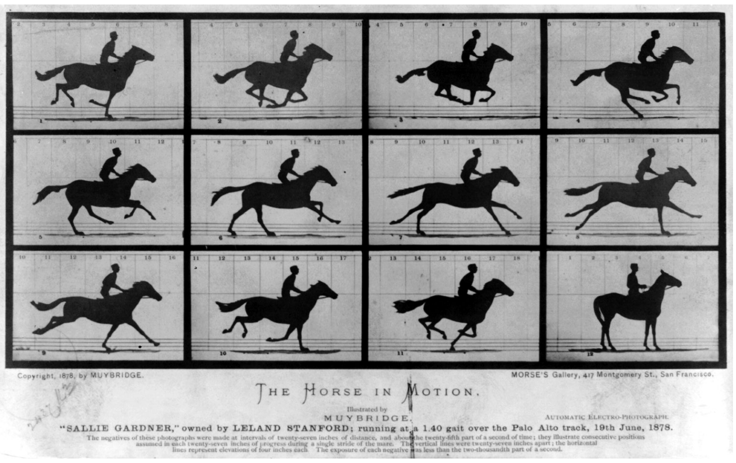

FIGURE 1.1: Muybridge's *The Horse in Motion*,1878 [47]. Notice the Horse *flying* in frames 2 and 3.

Pulsed lasers provide excellent temporal resolution, limited by the pulse width itself, on the order of 10^{-12} s to 10^{-18} s [11][43]. One of most the popular time resolved methods is pump-probe, which is presented in figure 1.2.

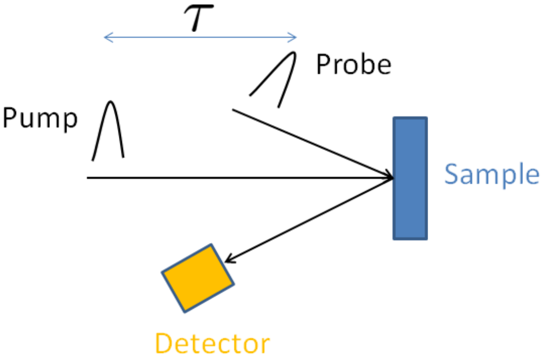

FIGURE 1.2: A typical reflection geometry pump-probe setup. τ corresponds to the time delay between the pump and the probe beams, as introduced by the delay stage. The pump beam excites the sample while the probe (less intense) measures the changes as a function of τ.

A typical pump-probe setup consists of a *pump* pulse and a *probe* pulse[*] derived from a single pulsed laser, with temporal widths ranging from picoseconds to femtoseconds. These pulses are focused onto the sample surface on the same spot, with a large pump:probe spot size ratio in order to probe a homogeneously excited region. Typical systems have a solid-state laser pumping Ti:Sapphire oscillator cavity to produce an 800nm pulsed output. As mentioned earlier, the two beams can be derived from the

---

[*] When the pump and probe pulses are in the same wavelengths, this method is called a *degenerate* pump-probe, otherwise the method is referred to as *non-degenerate* pump-probe. See for example [41]

same laser source by use of a beam splitter which is typically the case. Alternatively, one can also use two laser systems operating synchronously, producing fixed delays between the two pulses (see for example [42]). As the name suggests, the pump beam *perturbs* the sample and the probe is used to *investigate* the pump induced effects in the material. This can be done by probing the changes associated with the material properties such as the reflectivity(transmitivity). In addition to pulsed lasers, a central feature of pump-probe experiments is the *delay stage* which introduces a variable temporal delay between the pump and probe pulses, much smaller than the pulse width. Both of these are necessary to achieve the temporal resolution required to study ultrafast processes and thus jointly set the minimum temporal resolution. An illustration of these details is found in appendix A .

As pump-probe techniques are a powerful tool to understand the carrier dynamics, applying this to thermoelectrics could prove to be fruitful. Due to increasing energy demands and energy waste (partly in the form of heat), energy recovery is important. In this regard, thermoelectrics can be used to recover wasted heat. This may be seen as follows. Thermoelectrics are materials that convert heat into usable electrical energy. Figure 1.3 shows a typical thermoelectric generator consisting of n-type and p-type thermoelectric materials. A temperature gradient ΔT across the material results in the induced potential gradient (E_{emf}) and hence the observed current. This corresponds to the Seebeck effect,

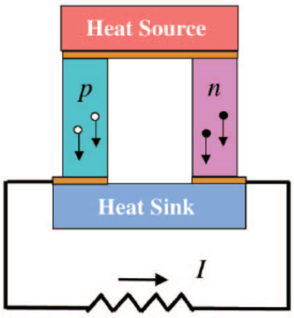

FIGURE 1.3: A thermoelectric generator [44].

$$E_{emf} = -S\Delta T \quad . \tag{1.1}$$

Here S is the Seebeck coefficient. Clearly, efficient functioning of such a device requires poor thermal conductivity to maintain a steady temperature gradient and a good electrical conductivity for the non-dissipative flow of current. Accordingly, thermoelectrics are characterized by thermoelectric figure of merit [44] (ZT) which characterizes the thermoelectric conversion efficiency;

$$ZT = \frac{S^2 T}{\rho \kappa}, \tag{1.2}$$

where κ is the thermal conductivity of the material, ρ corresponds to the material resistivity, S is the Seebeck coefficient, and T the temperature respectively. T is multiplied on either side to make ZT dimensionless. Since thermal conductivity involves heat transport and the associated carrier dynamics, it would make sense to understand the underlying mechanisms to optimize ZT.

In this regard, PbTe happens to be an excellent candidate. With a face centered cubic (FCC) lattice structure, the material has an exceptionally *low* (2 $Wm^{-1}K^{-1}$ at 300K) thermal conductivity [13]. In fact, under appropriate doping, it has a large Seebeck coeffiecient, excellent electrical conductivity and as such, a large ZT in the range of 1.4 to 3.4 [44] [25]. In general, ZT can be tuned by changing carrier concentration levels (**n**), effective mass (**m***), electronic ($\kappa_{\mathbf{e}}$) and, lattice thermal conductivities ($\kappa_{\mathbf{l}}$) [†]. The complexity involved has to do with the fact that all of these parameters are inter-related and they should be optimized simultaneously to achieve maximum ZT [39]. Recent inelastic neutron scattering (INS) experiments have revealed that the exceptionally low lattice thermal conductivity (κ_l) for PbTe may be due to an anharmonic interaction between TO and LA phonons in the material [13]. A major new assertion is that the LA mode softens due to the interaction with the soft TO mode. Thus, it would be interesting to study the material using time-resolved methods to investigate these phonon and carrier interactions to better understand the scattering dynamics on ultrafast time scales, and determine if LA mode screening can be seen.

In this experiment, we investigate the carrier relaxation and phonon dynamics in *undoped* PbTe by means of pump-probe spectroscopy. In this thesis, we report our observations on PbTe detailing the existance of coherent oscillations in reflectivity associated with phonon excitations. Further, we study carrier relaxation dynamics which demonstrate unusual e^--phonon coupling that manifests unexpected temperature dependencies that deviate from conventional semiconductors.

[†] There are multiple ways to tune this; alloying/creating vacancies, usage of complex structures or even, multiface composites [39].

Chapter 2

Theoretical Background

2.1 Ultrafast Charge Carrier Dynamics of Semiconductors

Ultrafast carrier dynamics in essence involves *momentum* and *energy* relaxation of the material from a non-equilibrium state during photoexcitation to an equilibrium state that exists in the absence of photoexcitation. This of course happens in accordance with the principle of conservation of energy and momentum.

In a semiconductor, when carriers are excited by pulsed radiation, both the electrons and the lattice absorb energy from the radiation. Subsequently, a non-equillibrium state is created between these systems due to their different specific heat capacities. The electronic specific heat is smaller than the lattice specific heat, and thus, the electrons are higher in temperature as compared to the lattice after the excitation process. Absorption of energy by electrons corresponds to a vertical interband transition leading to the creation of a hole in the valence band for every electron that populates the conduction band. This is followed by elastic and inelastic scattering processes between carriers typically occuring over 100's of femtoseconds (fs), to achieve momentum randomization and energy transport. This is followed by a quasi-equilibrium statistical distribution for the carriers. From here, the electron-zone center optical phonon interactions ($\leq 1\ ps$), optical phonon-acoustic phonon interactions ($8\ ps$-$20\ ps$) and, e^--hole recombination processes ($\geq 1\ ns$) occur and, eventually the system attains equilibrium. In figure 2.1, we provide a graphical summary of these processes are described. The time scale of these ultrafast processes in semiconductors are found in Table 2.1.

There are multiple approaches to model charge carrier dynamics. A *microscopic* description includes the *density matrix formalism* involving optical bloch equations describing time varying ensemble populations due to perturbation by the pump pulse [36] .

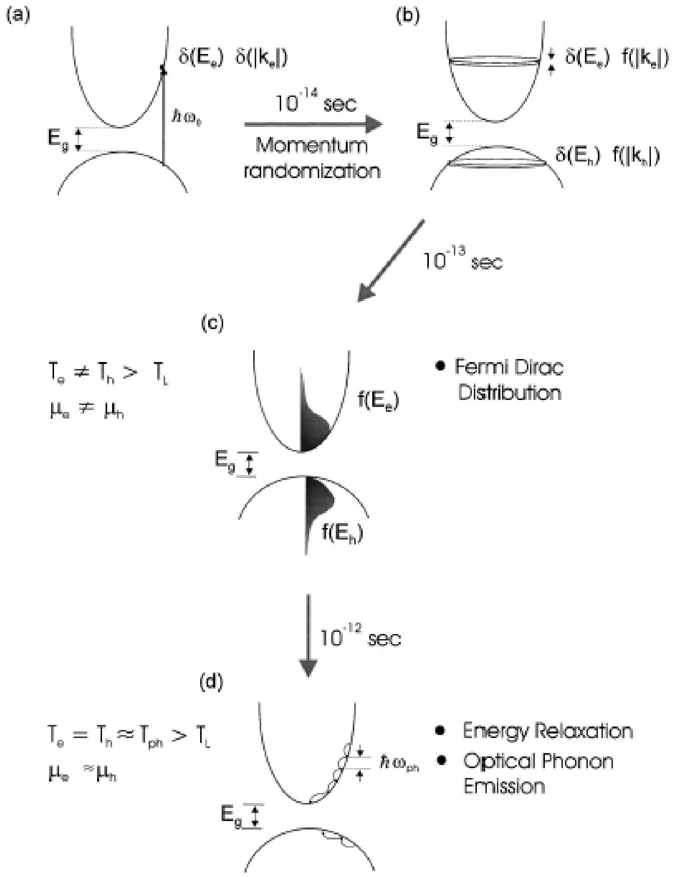

FIGURE 2.1: Ultrafast dynamics in a semiconductor, a hierarchy of events. A delta function distribution corresponding to the excitation energy results upon perturbation by the pump beam. This is followed by thermalization processes (momentum randomizations) that finally drives the system to equilibrium Fermi-Dirac (e^- and holes) and Bose-Einstien distributions (phonons), nevertheless, the lattice and carrier temperatures don't match yet. As a last step, the temperatures between these systems equilibrate (through emission of phonons) to attain ground state [31] .

One of the popular mean field approaches includes, for a non-magnetic system, a two temperature model which is essentially a set of coupled differential equations in temperature for the subsystems involved and, based on the strength of the coupling between these subsystems, the relaxation times so determined vary accordingly (this mostly models the heat flow dynamics/ultrafast thermal response in the material, see for example [8]). The latter model will be discussed in section 2.1.4 .

2.1.1 Interband Transitions in Semiconductors

Absorption edge for semiconductors typically fall in the near-infrared and visible regions of the spectrum. The absorption spectra of PbTe is shown in figure 2.2. For PbTe

TABLE 2.1: **Time order of Ultrafast processes in Semiconductors.**

Time Scale	Relevant Process	Remark
10-100fs	Optical excitation of carriers through interband transitions	Excitation time scale is proportional to the pulse width
10-100fs	Coherent regime	-
<200fs	Nonthermal regime, mostly momentum randomizations occurs through $e^{-}-e^{-}$ scattering	The system is in a non-equilibrium state, cannot be described by equillibrium distribution functions yet
100fs-ps	Hot carrier regime, $e^{-}-e^{-}$ scattering and e^{-}-phonon scattering begin to happen	The carriers can be described by a well defined temperature by now, distribution functions are well defined in this regime
ps-μs	Isothermal regime, dominated by $e^{-}-h$ recombinations	The sytem on the whole attains an equilibrium temperature; Lattice and the carrier sub-system temperatures are equalized

single crystal samples (curves A and B in figure 2.2), the absorption maximum is in the UV-visible and has an absorption edge at 4 μm.

The infrared absorption is related to the excitation of vibrational degrees of freedom of the lattice while the UV-visible absorption in semiconductors (including PbTe) have to do with the interband transitions across the band gap by the valence band electrons. In fact, as the absorption edge defines the energy threshold at which the semiconductor starts absorbing light, this approximately coincides with the material band gap. For example, 4 μm corresponds to PbTe bandgap and this is also observable from the absorption spectra in figure 2.2.

Interband transitions are governed by *Fermi's golden rule* which is an application of time-dependent perturbation theory for transitions between continuum of states in the valence band $|\Psi_i\rangle$ (initial) to continuum of states in the conduction band $|\Psi_f\rangle$ (final). To first order [17],

$$W_{i\to f} = \frac{2\pi}{\hbar}.|\langle\Psi_{i\mathbf{k}}|\mathcal{H}'|\Psi_{f\mathbf{k}'}\rangle|^2.g(E), \tag{2.1}$$

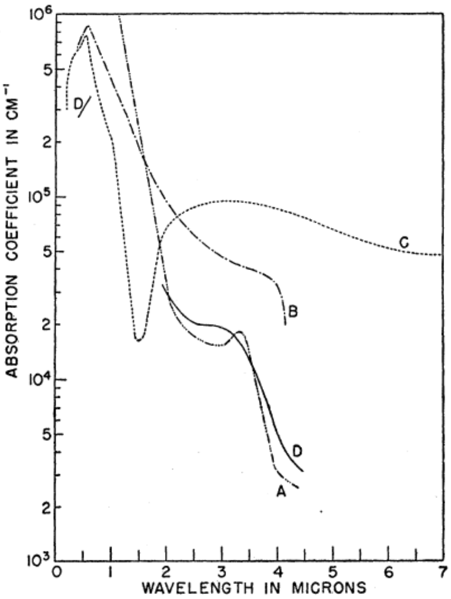

FIGURE 2.2: Absorption coefficient as a function of wavelength for thermoelectric semiconductor material PbTe. As discussed earlier, noticeable is the absorption maximum in the UV-visible (A,B). **A**-**D** are the results by different authors on crystals (A,B) and thin films (C,D) [38].

where $W_{i \to f}$ corresponds to the interband transition probability between the state $|\Psi_{i\mathbf{k}}\rangle$ in the valence band to the state $|\Psi_{f\mathbf{k}'}\rangle$ in the conduction band. i and f label the initial and final state band index corresponding to valence and conduction bands, respectively. $\mathbf{k}$ and $\mathbf{k}'$ label initial and final momentum state of the e^- within the bands i and f, respectively. $g(E)$ represents the *joint density of states* at the incident photon energy E, which is the probability that the initial and final states that are involved are available for transition/occupancy. $\mathcal{H}'$ is the Hamiltoninan that couples the states involved in the transition. For condensed matter systems, specifically for crystalline solids with Bravias lattices, the electronic states(in position space) are described by Bloch functions,

$$\Psi_{n\mathbf{k}}(r) = e^{-i\mathbf{k}.\mathbf{r}}.U_{n\mathbf{k}}(r), \tag{2.2}$$

where n labels the band index (i and f in the earlier discussions), $\mathbf{k}$ represents the momentum state within the band n. $U_{n\mathbf{k}}(r)$ is the wave function bearing the symmetries of the atomic orbitals involved and modulates the plane wave solution. This function has the periodicity of the lattice. Intuitively, one can imagine the transition from free electron gas model, those which have planes waves as a solution, to electrons in a periodic potential of the lattice that introduces semi-localization for electrons and the subsequent modulation of the plane waves. The periodicity is reflected by the periodicity of the lattice potential itself[*]. Thus, based on the functional form of $U_{n\mathbf{k}}$ and $\mathcal{H}'$, one can deduce selection rules for driving perturbative interband transitions which is evident from the following equation,

$$|\langle i\mathbf{k}|H'|f\mathbf{k}'\rangle| \propto \int d^3\mathbf{r}\,U^*_{i\mathbf{k}}(\mathbf{r}).\mathcal{H}'.U_{f\mathbf{k}'}(\mathbf{r}) \ . \tag{2.3}$$

Depending on the symmetry of $U_{n\mathbf{k}}$ and $\mathcal{H}'$, the above integral can have non-zero values (in mathematical terms, this should be an even inetgral).

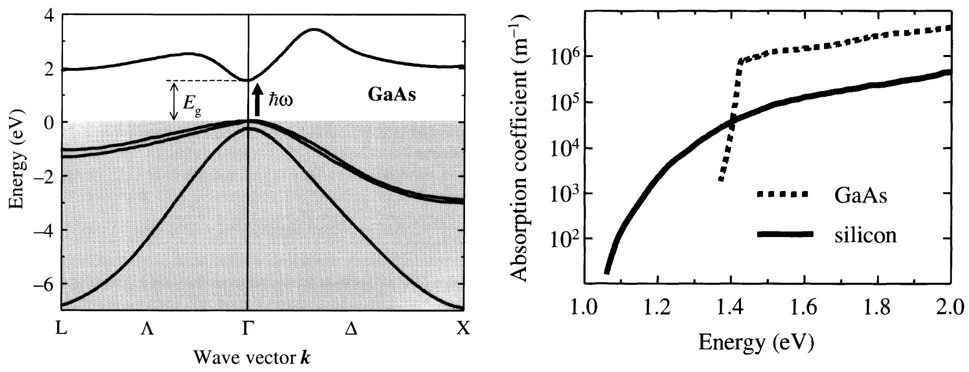

Figure 2.3: Left: Band structure of GaAs. GaAs has a direct band gap of 1.42eV(E_g) which also defines the absorption edge. Right: A comparison of α for GaAs and Si. Si has a direct gap at the Γ of 3.4eV and an indirect band gap of 1.12eV. Noticeable is the beginning of the absorption starting from right around $\approx$ 1.1eV, as somewhat a smooth absorption profile in contrast to GaAs which has a roughly step-function like behaviour. The smoothness has to do with phonon assisted transitions that impart big changes in $\mathbf{k}$, that make the transitions still possible at $<\Gamma$-point energies [17].

These transitions could occur across direct or indirect band gaps depending on the material. Materials which have the conduction band minima and valence band maxima at the *same* $\mathbf{k}$ constitute direct gap materials and those for which they do not coincide at the same $\mathbf{k}$ are indirect band gap materials. Indirect band transitions are usually phonon assisted as the $\mathbf{k}$ associated with photons cannot bring about big changes in the electronic momentum. Thus, it is clear that phonon populations could play a deciding role in absorption features beyond the absorption edge for indirect gap materials. A mere comparison between these two types of semiconductors can reveal a great deal of information about the electronic band structure. As an example, the effects due to differences in band structures have been shown in Figure 2.3 for prototypical semiconductors, GaAs and Si.

---

[*] Simplest of models in this regard(of e^-'s in periodic potential) include, for example, the Kronig-Penny model, of electrons in periodic square well potential.

2.1.2 Relaxation Schemes

Once the conduction band is populated, the system is in non-equilibrium state. Energy re-distribution among the electronic and lattice subsystems is required to relax the system towards equilibrium. Each of these subsystems have their characteristic interaction time scales to distribute energy within and between the subsystems. A brief summary of the relaxation scheme is already discussed in Figure 2.1 and the introduction that followed. Figure 2.4 shows the general order of processes once the carriers are excited, considering GaAs as an example. Also shown is the evolution of phonon population, leading to an eventual energy relaxation of the material to the ground state.

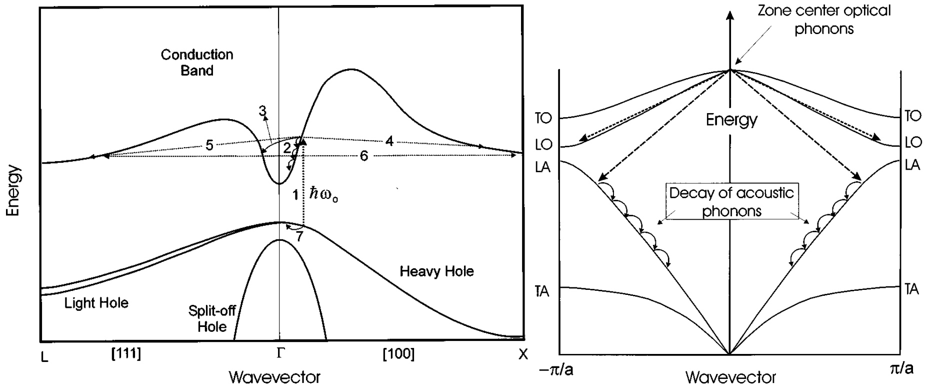

FIGURE 2.4: Left: Energy relaxation in GaAs. **1** signifies photo-excitation, followed by inter-(**4** – **6**) and intravalley (**2** – **3**) inelastic scattering generating Optical ((2)) and acoustic phonons ((3)). **7** is an intravalley relaxation of the hole population. Right: Energy distribution order in the lattice sub-system. As can be seen, high energy optical phonons so generated (see figure on the Left) scatter off low energy ones and eventually the lattice system reaches an equilibrium temperature [31] .

The electronic subsystem cools down rapidly ($\approx 100\ fs$) by inelastic collisions between the constituent electrons and reaches a quasi-equilibrium temperature (T_e), greater than the lattice temperature $(T_l)^\dagger$. This state is characterized by Fermi-Dirac distribution. The quasi-equilibrium breaks down due to interband transitions ($\approx 1\ ps$) that follow by the emission of zone center longitudnal and transverse optical phonons (e^--LO and e^--TO interactions). This is followed by optical phonon-acoustic phonon interactions as well as e^--transverse/longitudnal acoustic phonon ($e^- - TA/LA$) interactions which happen on similar time scales (≈8 ps-20 ps).

Intervalley scattering accounts for a major portion of momentum transfer as this involves large **q**-vector phonons (LA/TA) while intraband scattering can emit zone center phonon modes with small **q**-vector phonons (LO/TO). In addition, relaxation can also

---

[†] The fact that $T_e > T_l$ corresponds to the system in quasi-equilibrium; eventually T_e and T_l should reach equilibrium temperature over time and hence, initial equilibrium state for electronic subsystem is only a momentary one.

occur through inter-zone scattering which involves the transfer of energy and momentum across adjacent brillouin zones[‡]. All in-elastic/elastic scattering processes (excluding the electron-electron scattering) constitute coupling between electronic and phonon sub-systems[§]. The energy transfer time scales vary based on the coupling strength between these subsystems. The relaxation scheme discussed here describes the back bone of ultrafast carrier recombination processes in a photoexcited semiconductors. There can also be other processes such as Auger recombinations, exciton shielding and, hot carrier effect that can prolong the relaxation process in a semiconductor (details of these processes can be found in [31]).

Given the unique thermal conductivity properties of PbTe, it makes sense to discuss the possible mechanisms of carrier-phonon and phonon-phonon interactions, as well as the kind of phonon modes involved and the corresponding interaction features. This is the subject of the section that follows (the discussion in the subsequent section is adapted from [3]).

2.1.3 e^--Phonon Interactions

For an ideal case of a crystalline condensed matter system, the Hamiltonian with Born-Oppenheimer approximation[¶] maybe written as,

$$\mathcal{H} = \mathcal{H}_{ions}(\mathbf{R_j}) + \mathcal{H}_{e^-}(\mathbf{r_i}, \mathbf{R_{j0}}) + \underbrace{\mathcal{H}_{e^- - ion}(\mathbf{r_i}, \delta\mathbf{R_j})}_{electron-phonon} \ , \tag{2.4}$$

where R_j and R_{j0} correspond to j^{th} ionic position and equilibrium ion position, respectively, while r_i's and δR_j's represent i^{th} electronic position and displacement of the j^{th} ion about it's equilibrium position R_{j0}. Of interest to us is the $\mathcal{H}_{e^- - ion}$ Hamiltonian. Zone center interactions primarily happen through deformation potentials and phonon mode induced polarization field-electron charge interactions. Zone edge interactions involves mostly the former interaction type. To first order, $\mathcal{H}_{e^- - ion}$ (considering the Hamiltonian expectation value) maybe written as,

---

[‡] These are also called an Umklapp process

[§] Spin relaxation is also a part of the energy exchange subsystem, specifically for magnetic materials(See for example, the *Three Temperature Model* [22]). This would have been a possible pathway in case PbTe were doped with a magnetic impurity; PbTe:Ti is magnetic [46].

[¶] This is the approximation that the ionic motion feels the average adiabatic potentials due to electron's and the electronic motion is in phase with that of ion cores; thus, in principle, from the e^- perspective, the ions are practically stationery.

$$\mathcal{H}_{e^- -ion} \approx \left[\frac{\partial E_{n\mathbf{k}}}{\partial R_j}\right]_{R_{j0}} .\delta R_j \ . \tag{2.5}$$

In arriving at the above equation, it is assumed that the electrons instantaneously respond to the ionic motion. $E_{n\mathbf{k}}$ represents the energy of an e^- in n^{th} band with wave vector **k**. Such changes in electronic energies are possible through lattice deformation introduced by phonons. This is apparent in the case of LA and TA phonons which are strain wave deformation of the lattice. This is most apparent in the case of LA and TA modes due to do the fact that they represent in-phase motion of the basis atoms (this approximation is valid only near the zone center) within an unit cell across the lattice while the optical branch represents out of phase motion (also close to zone center) of the basis atoms within unit cells.Thus optical modes can be approximated as microscopic deformation of the lattice[‖]. Accordingly one can associate a deformation potential to the phonons, which is also proportionality factor to the corresponding global band structural change in the material. In general, the material strain is the symmetric tensor of the lattice displacement gradient, given by

$$S_{ij} = \left[\frac{\partial(\delta R_i)}{\partial R_j}\right]_{symmetric} = \frac{1}{2}\left(\frac{\partial \delta R_i}{\partial R_j} + \frac{\partial \delta R_j}{\partial R_i}\right) \ . \tag{2.6}$$

Applying group theory tells us that S_{ij} is a reducible representaion of the strain tensor. Thus S_{ij} maybe expressed as a sum of Γ_1, Γ_3 and Γ_4 irreducible representations. Γ_{1-5} represent the irreducible representation of the crystalographic *point group* S_P^G[**] of a crystal at the Γ point. Γ_1 represents relative volume change ($\delta V/V$) component of S_{ij}, Γ_3 and Γ_4 represents shear component of S_{ij} due to uniaxial stress along [100] and [111] directions respectively. Equation (2.5) maybe used to deduce Hamiltonians for interaction involving deformation potential.

We first consider *zone center deformation potential interactions*, with long wavelength acoustic and optical phonons:

- **e^--LA interaction** Longitudinal modes corresponds to compressional waves in the material and these have $\delta\mathbf{R_j}$'s along the direction of the wave propagation **q**. On considering a periodic disturbance of amplitude $\delta\mathbf{R_0}$, with an oscillation

---

[‖] The analogy of macroscopic and microscopic oscillations is an approximate one and cannot be generalized; this can be seen as an approximate case of solution to 1D diatomic oscillator model, for example, see[s].

[**] S_P^G is a set of all symmetry operations on the crystal that preserve it's structure. A crystallographic point group can be mapped to a group consisting of matrix representation of the elements of S_P^G which forms the representation of the point group. These representations can be reducible or irreducible based on their structure. For more details, one can refer [**?**]

frequency ω, equation (2.5) yields,

$$S_{ij} = \frac{1}{2}[q_i.\delta R_{j0} + q_j \delta R_{i0}].cos(\mathbf{q}.\mathbf{r} - \omega t) = q_i \delta R_{i0} = S_{ii} \ . \tag{2.7}$$

This is also proportional to the global change in the electronic energy, so that the Hamiltonian maybe expressed as,

$$\mathcal{H}_{e^- - LA} = \alpha_{n\mathbf{k}} \left(\mathbf{q}.\delta\mathbf{R}\right) \ . \tag{2.8}$$

In terms of Phonon creation and destruction operators,

$$\mathcal{H}_{e^- - LA} = \alpha_{n\mathbf{k}} \mathbf{q}. \sum_{\mathbf{q}} \left(\frac{\hbar}{2NV\rho\omega} \right)^{\frac{1}{2}} \mathbf{e_q} \left[d^{\dagger}_{\mathbf{q}} exp[i(\mathbf{q}.\mathbf{r_j} - \omega t)] + d_{\mathbf{q}} exp[-i(\mathbf{q}.\mathbf{r_j} - \omega t)] \right] \ . \tag{2.9}$$

N is the number of unit cells in the crystal, ρ the material density, V the crystal volume, $d_{\mathbf{q}}$ and $d^{\dagger}_{\mathbf{q}}$ represent phonon destruction and creation operators, $\mathbf{e_q}$ corresponds to phonon polarization unit vector, and $\alpha_{n\mathbf{k}}$ represents the deformation potential. From the Hamiltonian, it is clear that at high enough temperatures ($k_B T >> \hbar\omega$)[††], the matrix element of $\mathcal{H}_{e^- - LA}$ squared is independent of $\mathbf{q}$ implying a *short range interaction*. Also, $\mathcal{H}_{e^- - LA}$ depends on the mode frequency as $\sqrt{\omega^{-1}}$, and as we shall see, this can have a profound impact on the observed carrier dynamics of PbTe. One important feature of LA phonons is that, they preserve the symmetry of the crystal which accounts for their influence on the entire energy structure within the Brillouin zone. It should be noted that the above expressions have been derived considering non-degenerate bands. The case of degenerate bands is complicated and maybe found in [19].

- **e$^-$-TA interaction** TA phonons represent shearing rather than dilation in materials. Thus these modes, unlike LA phonons, do not preserve the symmetry of the lattice and lift the degeneracy of the otherwise non-degenerate bands. The interaction with electrons is still through deformation potentials, only that here, these correspond to proportionality constants for the energy gaps created at the band gap degeneracies.

- **e$^-$-TO** and **LO interactions** The optic branch of the phonons correspond to microscopic, longitudnal compression/transverse oscillations of the basis atoms across brillouin zones. The relevant Hamiltonian $\mathcal{H}_{Optic}$ is,

$$\mathcal{H}_{Optic} = D_{n\mathbf{k}}(u_{LO/TO}/a_0) \ , \tag{2.10}$$

[††] based on Bose-Einstein distribution of phonon occupation as dictated by the operators $d^{\dagger}_q$ and d_q

$u_{LO/TO}$ corresponds to lattice displacement due to LO/TO mode of the basis atom relative to one another, $D_{n\mathbf{k}}$ the associated deformation potential, and a_0 the equilibrium separation of the basis atoms. As is the case with all of the deformation potential based interactions discussed above, the absence of phonon **q**-vector dependency signifies the absence of long range interactions in dual space. As is the characteristic of deformation potential interactions, $\mathcal{H}_{Optic}$ is proportional to $\sqrt{\omega^{-1}}$. This characteristic dependence of the interaction Hamiltonian has significant role to play in case of materials which demonstrate the phenomena of *mode softening*. Mode softening is discussed in PbTe in section 2.3 and the related effects on PbTe carrier dynamics in section 3.2.

Zone center Phonon induced **E**-field-e^- interactions: *Piezoelectric* and *Frölich*

- **Piezoelectric Field interaction** In case of noncentrosymmetric materials such as PbTe [‡‡] , applied strain can induce **E** fields-the *Piezoelectric effect*. This can be generalized to the situation of periodic fluctuations in strain-Acoustic phonons. The induced field is given by,

$$\mathbf{E}_{Pz} = \mathbf{e}_m . \frac{\overbrace{\mathbf{q}\delta\mathbf{R}}^{S_{ij}}}{\epsilon_0\epsilon_\infty} \tag{2.11}$$

  where $\mathbf{e}_m$ is the electromechanical tensor of rank 3. Associating a scalar potential Φ_{Pz} with this field and using this, one can construct a Hamiltonian for the Piezoelectric field induced e^--Acoustic phonon interactions:

$$\mathcal{H}_{Pz} = -|e|\Phi_{Pz} = \frac{|e|}{\epsilon_0\epsilon_\infty q^2}\mathbf{q}.\mathbf{e}_m.(\mathbf{q}\delta\mathbf{R}) \ , \tag{2.12}$$

  ϵ_0 and ϵ_∞ are static and high frequency dielectric constants respectively. $\mathcal{H}_{Pz}$ has a q^{-1} dependence meaning that, this is a long range interaction in the real space.

- **Frölich interaction** This is an important kind of interaction in polar semiconductors. This involves LO phonon modes resulting in macroscopic fluctuations in the longitudnal electric field. The electrons then couple to these fields and exchange energy. The induced field corresponds to [34],

$$\mathbf{E}_{LO} = \sqrt{\frac{N\mu\omega_{LO}^2(\epsilon_\infty^{-1} - \epsilon_0^{-1})}{\epsilon_0}}\mathbf{u}_{LO} \ , \tag{2.13}$$

[‡‡] Ferroelectrics are known to generally exhibit *Piezoelectric effect*.

where μ is the reduced mass of the basis atoms within the primitive cell, N is the unit cell density, and ω_{LO} is the LO phonon frequency. Notice that the $\mathbf{E}_{LO}$ fluctuations are along the LO mode $\mathbf{q}$ vector. Upon associating a scalar potential to $\mathbf{E}_{LO}$, one can deduce $\mathcal{H}_{Fr}$, the interaction Hamiltonian to be [34]

$$\mathcal{H}_{Fr} = -|e|\Phi_{Fr} = (ieF/q)\mathbf{u}_{LO} \ . \tag{2.14}$$

Notice the q^{-1} dependence of the Hamiltonian (all the other q dependencies arising from F and $\mathbf{u}_{LO}$ cancel each other out, this can be seen from the explicit functional form of the Hamiltonian which is *not* shown here) which implies a long range interaction in the real space.

A simplified picture to understand $\mathbf{E}_{LO}$ is to consider LO mode oscillations as those between infinite planes, charged oppositely(which is the case with polar semiconductors). $\mathbf{E}_{LO}$ then corresponds to the electric field between these infinite planes which fluctuate with changing plane separation. This is identical to the case of an infinite plane capacitor with the plate separation changing and looking at what happens to the field between the capacitor plates.

The specific form of the Hamiltonian allows us to compute selection rules for e^--phonon interactions. This can be calculated based on the symmetries of the interacting e^- initial and final state wavefunctions and that of $\mathcal{H}_{e^- - ion}$ that couple the transitions.

Zone edge and near-Zone edge Phonon (short wavelength)-e^- interactions:

- These interaction are mostly limited to just deformation potential interactions. This is true because of the q^{-1} dependency of the $\mathbf{E}$-fields(as seen from the previous discussions). Since scattering across valleys within bands involve large momentum changes, owing to the fact that zone edge phonons have large $\mathbf{q}$-vector, they are capable of bringing about large $\mathbf{k}$ changes to e^-s and are thus responsible for the phenomena known as intervalley scattering. The Hamiltonian characterizing zone-edge interaction is,

$$\mathcal{H}_{iv} = \mathbf{e}_{b\mathbf{q}} . \frac{\partial H_{e^-}}{\partial \mathbf{R}} u \ , \tag{2.15}$$

where $\mathbf{e}_{b\mathbf{q}}$ represents the phonon polarization vector with b the branch number, $\mathbf{u}$ representing the oscillation amplitude and thereby relating to the interaction strength. The matrix element for the states coupled by the Hamiltonian is related to the deformation potential as,

$$D_{ij} = \frac{\langle n\mathbf{k}|\mathcal{H}_{iv}|n'\mathbf{k}'\rangle}{u} \ , \tag{2.16}$$

where n's and $\mathbf{k}$'s represent band index and the brillouin zone vector of the coupled states.

Essentially intervalley scattering is through deformation potential interactions.

2.1.4 Modeling Charge Carrier Dynamics

Up till now we have seen how an electromagnetic perturbation can drive interband transitions and the subsequent material equilibration, and the relevant time scales for these relaxation processes (2.1). In this section, we model a general pump probe signal to see how this reflects the material dynamics and how one can extract the relevant parameters of interest: *relaxation times*.

The pump probe signal in most cases is a reflectivity(R) or a transmitivity(T) based measurement. These optical constants are directly connected to the material band structure. To better understand this link, we start with the fact that for an electromagnetic radiation traversing through a medium (say along the z-direction) of refractive index $n(\omega)$ and an absorption coefficient κ (ω), the plane wave maybe described as[§§] [17],

$$\psi(z,t) = \underbrace{E_0.e^{i(i\frac{\kappa\omega}{c})}}_{Absorption}.e^{i(\frac{n\omega}{c}.z-\omega t)} = E_0.e^{i(\frac{\widetilde{n}\omega}{c}.z-\omega t)} \quad . \tag{2.18}$$

$\widetilde{n} = n(\omega) + i\kappa(\omega)$ is the *complex* index of refraction and this is related to the dielectric constant $\widetilde{\epsilon_r}$ as $\widetilde{n} = \sqrt{\widetilde{\epsilon_r}}$. From classical electromagnetic theory, one can deduce a relationship between $\widetilde{n}$, R, and T as (only the results are shown here) citeMark,

$$R(\omega) = \left|\frac{\widetilde{n}(\omega) - 1}{\widetilde{n}(\omega) + 1}\right| \tag{2.19}$$

and

$$T(\omega) = \frac{2}{1 + \widetilde{n}(\omega)}. \tag{2.20}$$

Now, ϵ_r depends on the inner products of Bloch envelope wave functions between the states available for electronic transition (between valence and conduction bands) and corresponding occupation numbers[¶¶] [18],

---

[§§] Absorption happens in accordance with the Beer Lambert's law

$$I(z)|_{z=L} = I_0.e^{-\kappa L} \tag{2.17}$$

L the length of the medium through which the radiation traverses and I_0 the intensity at the surface of incidence(z = 0).

[¶¶] These are semiconductor specific relations, a contextual illustration. Also see [16] [21]

$$\epsilon(q) = 1 - \frac{4\pi e^2}{q^2} \sum_{k'} \sum_{k} \left| \langle k \left| e^{-i\mathbf{q}.\mathbf{r}} \right| k' \rangle \right|^2 \frac{(N_{k'} - N_k)}{(E_{k'} - E_k)} \quad . \tag{2.21}$$

N_k is the occupation number of the state $|k\rangle$, $\mathbf{q}$ is the electron wave vector, E_k is the energy of the k^{th} state. A pump-probe signal measures the differential reflectivity or differential transmitivity ($\frac{\Delta R}{R}$ or $\frac{\Delta T}{T}$) which is essentially a measure of change in the permitivity. Since this measurement is done as a function of various time delay, a pump-probe signal represents the change in $\widetilde{\epsilon}_r$ as a function of time. This is evident from the fact that occupation numbers change when one optically drives interband transitions. So, in essence, a pump-probe signal reflects a dynamic change in the electronic structure of the material.

Having considered equation (**2.21**), it can be seen that $\epsilon_r(q)$ is also dependent on the energy levels being populated and hence imposes on the reflectivity signal, a wavelength dependency. Thus, non-degenerate (for *white light*) pump-probe would reveal a great deal about the relevant carrier dynamics happening over the spectrum of the probe.

Now that we have an understanding of the underlying physics of pump-probe spectroscopy, we turn our attention to how one can extract relaxation time constants for the relevant scattering mechanisms based on mathematical modeling. It is evident from Figure 1.2 (**b**) that a typical pump-probe signal (in the reflection geometry [***]) shows temporal decay. Thus, it is natural to model (adapted from [2]) the actual system response (S_{res}), in most cases, as a sum of decaying exponentials,

$$S_{res} = \theta(t). \left[\sum_{i=c-c,c-ph,...} A_i.e^{-t/\tau_i} \right] \quad , \tag{2.22}$$

where $\theta(t)$ is a unit step function. The step function prompts an instantaneous response from the system to the induced perturbation. The Measured signal(S_{mes}) however is a convolution of S_{res} with the pump-probe auto-correlation function,

$$S_{mes} = \sum_{i=c-c,c-ph,...} \frac{A_i.e^{\frac{(-4\tau_i.t+2.\sigma^2)}{4.\tau_i^2}} .\sqrt{\pi}.Erfc\left[\sqrt{\frac{1}{2\sigma^2}} \frac{(-2\tau_i t+2\sigma^2)}{2\tau_i}\right]}{2\sqrt{\frac{1}{2\sigma^2}}} \quad . \tag{2.23}$$

In the summations above c-ph represents a carrier-phonon interaction channel. Figure 2.5 shows the effect of pulse width (σ) on the observed signal (S_{mes}). For the purpose of illustration, we've considered the summation equation (2.22) to consist of two

---

[***] Also applicable to the kinematics of the system studied with transmission geometry.

components, 1 ps (τ_1) and 10 ps (τ_2). It is seen that, whenever $\tau/\sigma >> 1$, the component is well resolved. This tells us that, in order to resolve the system response, the pulse width should be much smaller than the corresponding response.

In principle, one could also include ph-ph terms and slow heating terms in S_{res}. Moreover, in most applications of interests, the c-c channel is difficult to resolve because of the timescales of the process ($< 100\ fs$ typically). So, most cases, one would be measuring the e-ph and the ph-ph decay. To complete the picture, a third long lived component ($\approx 1\ ns$ or greater) is introduced to account for the slow equilibration through processes such as Auger recombination or carrier diffusion.

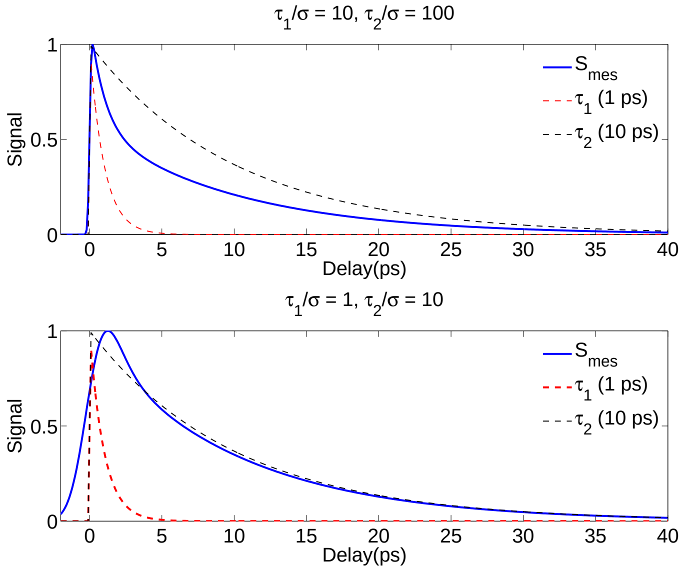

FIGURE 2.5: The system response S_{mes} for different pulse widths. Top: the 1 ps (τ_1) component is well resolved for $\frac{\sigma}{\tau_1} = 10$. Bottom: for $\frac{\sigma}{\tau_1} = 1$, τ_1 is unresolved while τ_2 is still well resolved.

For ultrashort pulses on the order of 10s of femtoseconds in duration, the pulse maybe approximated as a delta function and relaxation times maybe obtained by fitting just the decaying of the differential signal to equation (**2.23**), and extract appropriate time constants.

Finally, we briefly mention the *two temperature model* (TTM). The TTM is applicable when the electronic system has reached a quasi-equilibrium(section 2.1.2), to model the e^{-}-phonon interaction. This model considers two systems, lattice and the electronic subsystem at different temperatures and describes the energy exchange between the two. TTM is mathematically described by a set of coupled differential equations for T_e and T_l [24],

$$\gamma_e T_e \frac{dT_e}{dt} = \frac{(1-R)Fp(t)e^{-\frac{z}{d}}}{d} - \overbrace{U_{e-ph}(T_e, T_l)}^{e^{-}-phonon\ coupling} \tag{2.24}$$

$$C_l \frac{dT_l}{dt} = \underbrace{-C_l D \frac{d^2 T_l}{dz^2}}_{diffusion} + U_{e-ph} \ . \tag{2.25}$$

In equations (2.25) and (2.26), D, F, γ_e, C_l and, p(t) represent the thermal diffusion co-efficient of the material, pump fluence, electronic specific heat, lattice specific heat, and pump pulse-profile, respectively. R and d are the reflection co-efficient and the penetration depth at the central pump wavelength. $U_{e,ph}$ is the energy coupling between the subsystems. $U_{e,ph}$ is proportional to the e-phonon coupling coefficient, g_∞, and corresponds to a fit parameter that has to be determined from fitting a pump-probe dataset. Note that this model assumes electronic interaction with a single phonon subsystem. It should be noted that this model ignores the fact that there could be phonon-phonon interactions, electron-acoustic phonon interactions in addition to relatively fast electron-optical phonon interactions.

2.2 Optically induced Coherent Phonons

Lattice vibrations in a crystal can be modeled as a quantum harmonic oscillator. Let us consider a particular phonon mode at a frequency ω. In the absence of external perturbations, the expectation values of the conjugate variables P and Q ($\langle P \rangle$ and $\langle Q \rangle$) are zero. However, in the presence of a perturbation, mainly an impulsive driving force, the lattice can exhibit coherent oscillations. In general we'll be concerned with two types of oscillations namely coherent phonons and squeezed phonons. Before we understand these oscillations quantum mechanically, it would be beneficial to discuss it qualitatively.

To begin, consider a classical harmonic oscillator. In the absence of any perturbation, this oscillator can be represented in phase space as a point at the origin as shown in figure 2.6 (a). An impulsive perturbation to the oscillator corresponds to a non-zero momentum state and this is represented in phase-space as a point displaced from origin along the P axis by an amount P_0. The oscillatory motion due to the initial impulse can be represented as a point orbiting the origin at a radius P_0 with an angular frequency ω. This corresponds to the oscillations between state of zero position and zero momentum, the latter corresponding to the classical turning points.

A thermal distribution of phonons prior to an impulsive perturbation can be represented in phase-space as a shaded circle as shown in figure 2.6(a). Here, the diameter is related to the uncertainty in P and Q. The excitation of a coherent phonon through an impulsive excitation corresponds to the shaded circle being displaced along the momentum axis by some value P_0. The subsequent time evolution is represented by the circle orbiting the origin at a frequency ω (figure 2.6 (b)). As such, the expectation value of the position oscillates sinusoidally, that is the macroscopic oscillation of the lattice. A coherent phonon still represents a minimum uncertainity state, and though the $\langle Q \rangle$ oscillates, $\langle Q^2 \rangle$ remains unchanged [**?**].

The case of a squeezed state is markedly different. The impulsive excitation in this case does not involve a momentum displacement, but rather a "squeezing" of the phase space circle into an ellipse (figure 2.7). This ellipse then rotates about the origin at ω. Here, the major axis of the ellipse aligns with the Q axis twice per rotation, and so too does the minor axis (the same is true for the P axis as well). As such, though the $\langle Q \rangle = 0$ (the center of the ellipse is not displaced), $\langle Q^2 \rangle$ varies at 2ω (as does $\langle P^2 \rangle$). Thus, a sqeezed state does not correspond to a macroscopic oscillation of the lattice, but an oscillations of the variance of the lattice atom positions [**?**].

Mathematically, the origins of coherent oscillations can be understood by considering the susceptibility of the medium. The susceptibility (χ) of a medium depends on the phonon coordinate q. As such, we can Taylor expand it as [**?**],

$$\chi(t) \approx \chi_0 + \left[\frac{\partial \chi}{\partial q}\right]_0 q(t) + \left[\frac{\partial^2 \chi}{\partial q^2}\right]_0 q^2(t) + \ldots \quad . \tag{2.26}$$

The second term is associated with coherent phonons and the third with squeezing. We can model both systems as a driven harmonic oscillator (ignoring damping for simplicity) [**?**],

$$\ddot{Q} + \omega^2 Q = F(t) \ , \tag{2.27}$$

where F(t) represents the impulsive driving force. In case of coherent phonons, the driving force corresponds to,

$$F(t) = \left[\frac{\partial \chi}{\partial q}\right]_0 |\mathbf{E}(t)|^2, \tag{2.28}$$

where $\mathbf{E}(t)$ corresponds to the electric field of the pump pulse which impulsively drives the coherent oscillations. In the case of squeezed phonons,

$$F(t) = \left[\frac{\partial^2 \chi}{\partial q^2}\right]_0 q(t)|\mathbf{E}(t)^2| \tag{2.29}$$

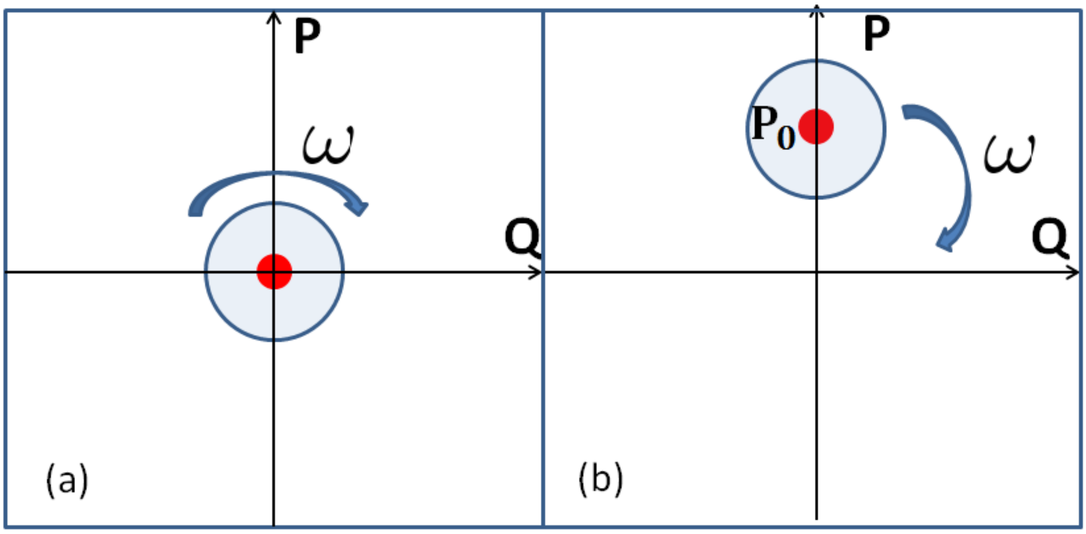

FIGURE 2.6: (a) In the absence of any perturbations, the phase space coordinate for a classical oscillator is represented by the red dot at the origin. Quantum mechanically, an unperturbed oscillator is represented by the shaded circle about the origin representing the uncertainty in P and Q (b) An impulsive perturbation results in new displased P coordinate for the oscillator, represented by P_0. For the quantum oscillator, this would mean $\langle Q \rangle$ is a non-zero quantity.

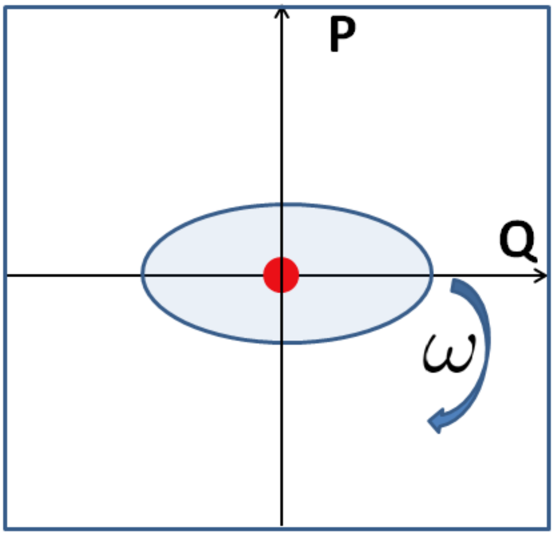

FIGURE 2.7: An impulsive excitation resulting in the squeezing of the uncertainties in the Q and P coordinates. Notice the average values of the phase space variable are still zero in this case ($\langle P \rangle = \langle Q \rangle$). Thus, what we observe essentially is a non zero variance in coordinates P and Q.

A squeezed phonon generally involves a coupling between two phonons from the same branch or between different branches [greg]. The latter corresponds to interbranch squeezing. It can be shown that the expectation value of the variance for such a squeezed state is [**?**],

$$\langle Q_1 Q_2 \rangle(t) = \mathcal{A}_+ sin[(\omega_1 + \omega_2)t + \phi_+] + \mathcal{A}_- sin[(\omega_1 - \omega_2)t + \phi_-] \ , \tag{2.30}$$

where ω_1, ω_2 are the two phonon frequencies, ϕ_+, ϕ_- represent the phase terms, $\mathcal{A}_+$, $\mathcal{A}_-$ are the amplitudes corresponding to $\omega_1 + \omega_2$ mode and $\omega_1 - \omega_2$ mode, respectively. These amplitudes are related to the Bose-Einstein distribution of the individual phonon modes [**?**],

$$\mathcal{A}_+ \propto 2 + n(\omega_1, T) + n(\omega_2, T) \tag{2.31}$$

$$\mathcal{A}_- \propto n(\omega_1, T) - n(\omega_2, T) \ , \tag{2.32}$$

where,

$$n(\omega, T) = \frac{1}{1 + exp(\frac{\hbar\omega}{k_B T})}, \tag{2.33}$$

is the Bose-Einstien distribution function for phonons at frequency ω, temperature T. It is clear that as the temperature becomes smaller, n becomes small. This means that the $\mathcal{A}_+ \rightarrow 2$ while $\mathcal{A}_- \rightarrow 0$. The difference mode becomes less prominent at lower temperatures while the sum frequency mode has an appreciable amplitude at low temperatures.

2.3 Lead telluride

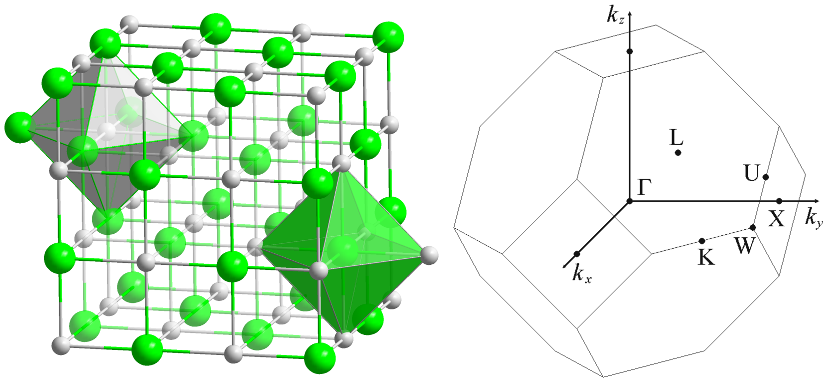

Figure 2.8: Crystal structure in direct and reciprocal spaces for PbTe. Left: PbTe has a FCC(Halite/Rock salt) structure, green represents Pb^{2+} and grey the $Te^{2-}ions$, each of these ions are surrounded by 6 of the other type in an octahedral fashion [33] . Right: The material first Brillouin zone [32] .

PbTe is a notable thermoelectric with a cubic(*halite*) lattice structure. The thermoelectric peculiarities and the corresponding enhancement schemes are already discussed in the introductory section of this thesis. To summarize, PbTe happens to possess an exceptionally low thermal conductivity, despite it's simple lattice structure, in the absence of alloying or any appreciable impurity based phonon scattering mechanisms.

The lattice structure and the first brillouin zone is shown in figure 2.8 and the reflectivity data in figure 2.9. The observed peaks in reflectivity correspond to the transition noted in the caption. These transitions are between p-like states for $E_1 - E_3$ and p-like Valence band and s-like Conduction band states for $E_4 - E_6$ transitions. A more detailed discussion on this maybe found in [7] [23].

PbTe has a direct band gap (E_g) of 0.3 eV at the L-point making it a narrow gap material. Figure 2.10 shows the band structure in the relevant subsection of the first brillouin zone. In the context of our experiments, it is important to consider change in the band gap due to temperature. In general, the gap of most semiconductors increases with decrease in temperature. This maybe noted from Figure 2.11 for prototypical semiconductors Si and GaAs.

Band gap changes with temperature can be associated with e^--phonon interaction and volume changes in the lattice [30],

$$\left(\frac{\partial E_g}{\partial T}\right)_p = \left(\frac{\partial E_g}{\partial T}\right)_{EP} + \left(\frac{\partial E_g}{\partial T}\right)_{TE} \tag{2.34}$$

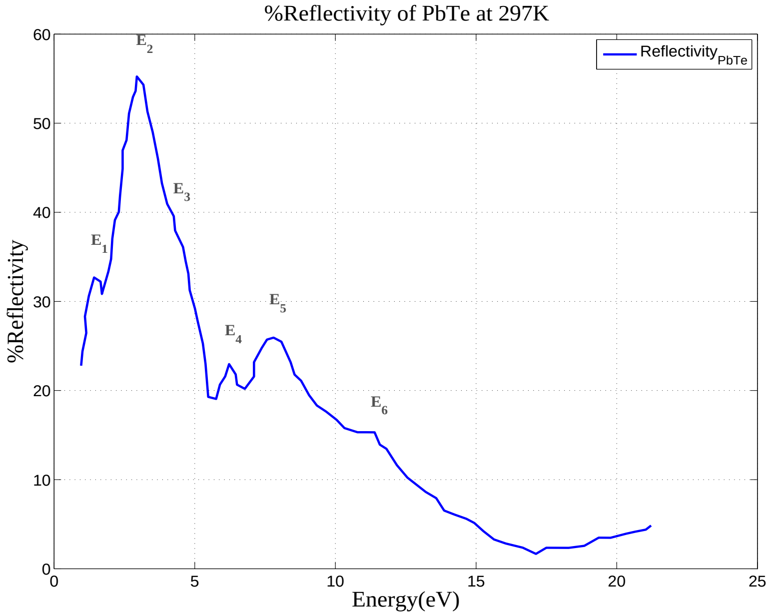

FIGURE 2.9: PbTe Reflectivity at 297K. E_{1-6} represents specific transitions in PbTe; $\Sigma_1 - \Sigma_4$ along band minimum in the $\Gamma - K$ zone, $\Delta_1 - \Delta_1$ between saddle points in the $\Gamma - X$ zone and zone edge $X_{5'} - X_2$ transition corresponds to E_{1-3} peaks in reflectivity. E_4 and E_5 peaks are representative of transitions at Γ and E_6 corresponds to L_3–$L_{2'}$ [7] .

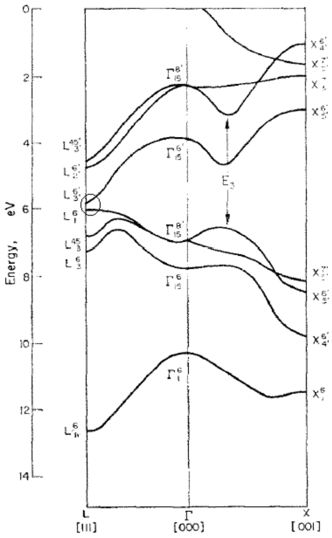

FIGURE 2.10: PbTe Band structure [12]. The material has at the L-point, a direct band gap($\approx 0.32eV$), the $L_1^6 \rightarrow L_1^{6'}$ direct transition(circle denotes the band gap) is thus possible for appropriate wavelengths.

subscripts p, EP, TE are constant pressure, electron-phonon-component, and thermal expansion component. It is found that, for PbTe, both TE and EP terms are positive.

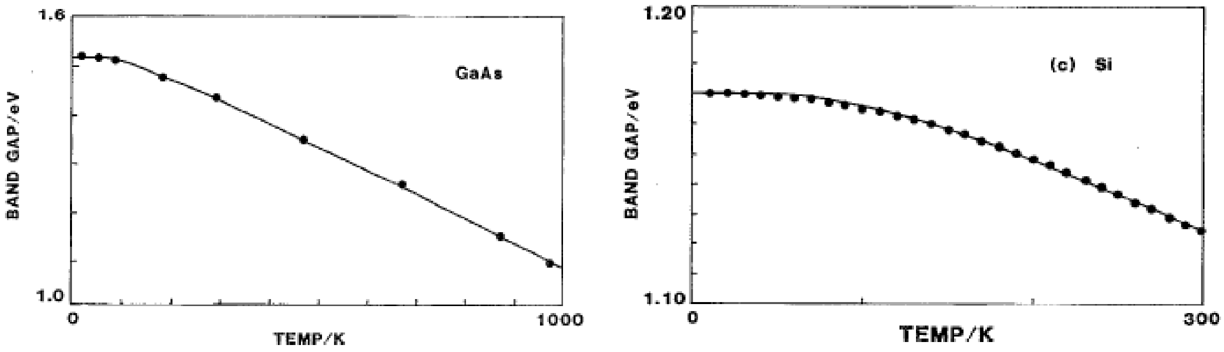

FIGURE 2.11: Temperature dependence of band gap for some common semiconductors. Left: GaAs. Right: Si. Both of them show a decrease in band gap with increase in Temperature [29] .

The band structure picture presented in Figure 2.10 doesn't take into account the spin-orbit interactions(**SO**) in PbTe. A more rigorous calculation of band structure taking into account spin-orbit interactions can be found in Figure 2.12 wherein, it can be seen the bandgap transition involves $L_6^+ \longrightarrow (L_4^-, L_5^-)$ states. Thus, the valence band involved in the transition at the band gap (L_6^+) is *not* an absolute valence band extremum. It is hypothesized that the L_6^- state that can *perturb* the L_6^+ state to cause the observed temperature trend associated with the EP interaction [7] . The forbidden $L_6^- \longrightarrow (L_4^-, L_5^-)$ transition is due to the parity of the bands involved and the associated selection rule.

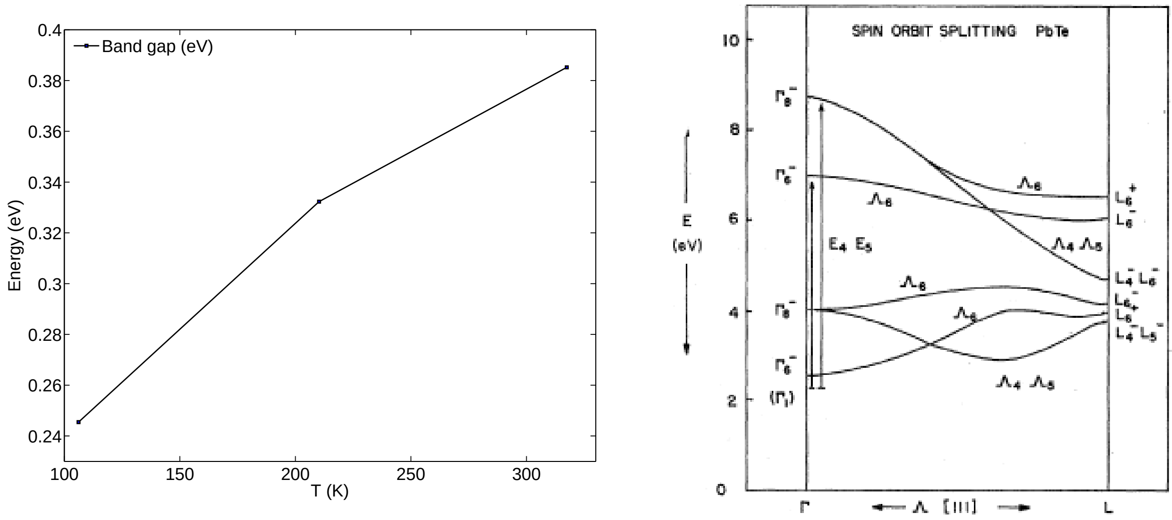

FIGURE 2.12: Left: Variation in PbTe Band structure with Temperature. This is based on a theoretical calculation, supplemented by X-ray diffraction studies [20]. Right: PbTe band structure(Γ-L zone) calculation with spin-orbit coupling taken into account. The band gap transition is between L_6^+ and (L_4^-,L_6^-) bands. Notice the valence band state L_6^- in between the bands involved in E_g transition [7] .

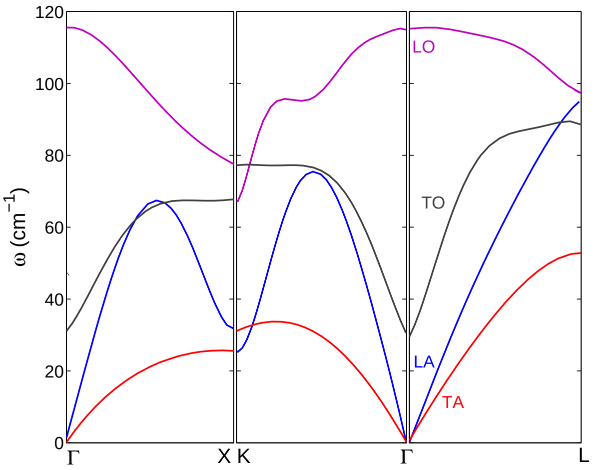

Figure 2.13: Experimental phonon dispersion relation of PbTe [10]. Notice the unusually low TO mode frequency at the Γ and the TO-LA crossing in Γ-X region of the brillouin zone (at approximately 60 cm^{-1}).

Figure 2.13 shows early experimental phonon dispersion relation for PbTe. The TO mode frequency at the Γ is smaller than in most semiconductors (GaAs for example [45]). However, as we shall see later, more recent experiments [13] reveal that there is great deal of ambiguity in phonon dispersion relation at the Γ point. This is partly due to the fact that PbTe also exibhits TO mode softening [1], meaning that the frequency of the TO mode close to the Γ point lowers with lowering temperature. However, the mode does not soften completely making PbTe a *paraelectric* [5]. In figure 2.14 one can find inelastic neutron scattering data showing mode softening in PbTe. The INS data also shows that the ω_{TO}^2 close to Γ has a linear dependence on temperature. This is referred to as the *Curie law* temperature dependence [9],

$$\omega_{TO}^2(\mathbf{q} \approx 0) = \gamma(T - T_c) \ , \tag{2.35}$$

where T_c denotes the *Curie temperature* which is the temperature at which the mode completely softens($\omega_{TO}^2 \to 0$)for ferroelectrics. The fact that TO mode follows Curie law(although not soften entirely at the Γ) makes PbTe a potential ferroelectric upon introducing some impurities/dopants, typically, Sn. As such PbTe is commonly referred to as an incipient ferroelectric.

Owing to the anomalous nature of the phonons at the Γ point, recent inelastic neutron scattering experiments on PbTe have revealed great deal of ambiguity in phonon dispersion. This may point to the origins of low κ_l in the material [13]. The argument

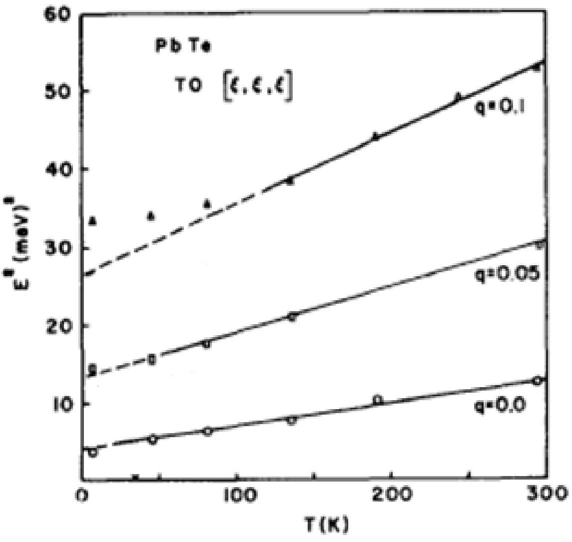

Fig. 2. Square of the TO mode energy plotted versus temperature for various values of reduced wavevector *q*.

Figure 2.14: Inelastic neutron scattering data representing mode softening in PbTe. The mode softening exhibits a linear trend with temperature, the so called *Curie law* temperature dependence [1].

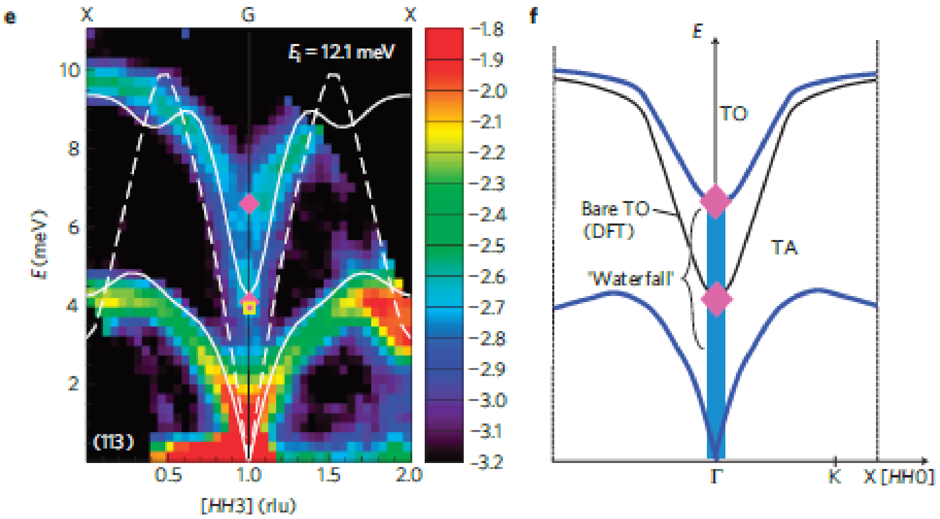

Figure 2.15: The *waterfalleffect* in PbTe. Left: The white lines are the DFT(Density Functional Theory) calculations of phonon dispersion relation for PbTe(in the Γ(G)-X zone). The dashed white line is the LA mode. Notice that the color coded data deviates from the DFT calculations; the LA mode happens to have a crossing with the TA mode close to the X point(≈ 4 *meV*, 0.2(*rlu*)) and the mode intensity seems to be extinguished in the Γ-close to X point regions(between 0.4(*rlu*) and 1.0(*rlu*)). Right: TA mode shifts in energy along the blue solid rectangle shows the TO mode to be at a low energy close to Γ [13]

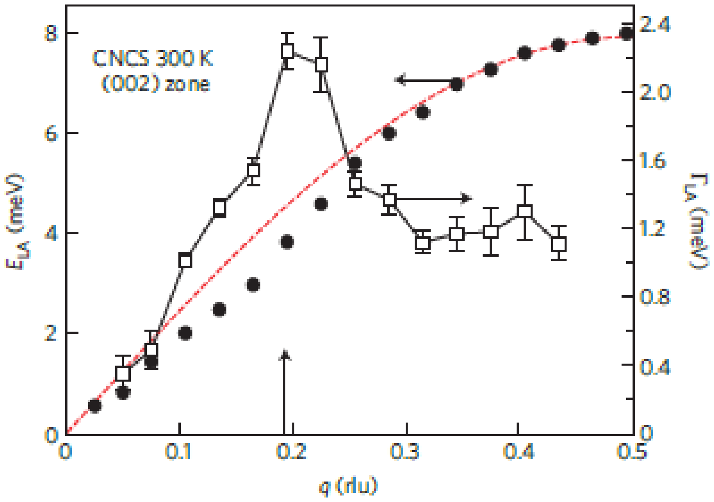

FIGURE 2.16: The experimental dispersion relation for LA mode. Notice the kink at $0.2\times\frac{2\pi}{a}$, a is the lattice constant [13].

is that the TO mode has a strong *anharmonic* coupling with the LA mode and the TO mode frequency may lie much lower at the Γ point than previously reported in figure 2.13 [10]. It is suggested that this strong anharmonic interaction softens the LA mode close to the zone center manifesting as a kink in the dispersion at $0.2\times\frac{2\pi}{a}$ where a is the lattice constant, as shown in figure 2.16. This effect of TO-LA mode coupling through an anharmonic interaction and the resultant softening of the LA phonon frequency is analogous to the *waterfall effect* seen in ferroelectrics. This ultimately results in lower group velocity for the LA mode close to the Γ point and maybe the source of the unusually low thermal conductivity in PbTe. Additionally, due to the repulsion between the LA and the TO modes, it is reasonable to expect that LA mode softens as well. As we shall see later, the phonon frequency plays a major role in determining the strength of e^- phonon interactions. As such, these unique properties manifest in the ultrafast relaxation dynamics.

Chapter 3

Experimental

3.1 The Experimental Setup

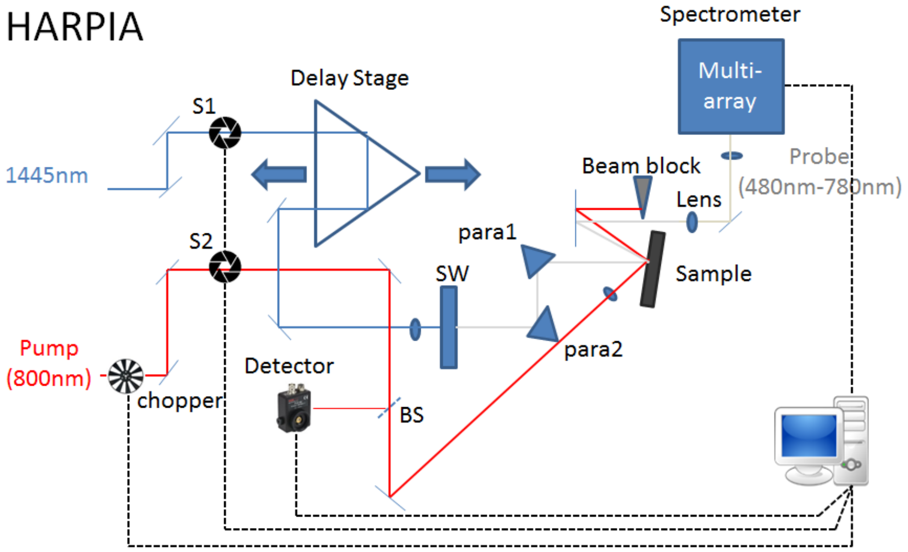

FIGURE 3.1: The HARPIA spectral pump-probe transient spectrometer. The red marker represents the pump beam path. The probe beam is a white light supercontinuum. To generate the continuum the 1445nm beam is focused onto the sapphire crystal(SW) and, it has a spectral band width ranging from 480nm-780nm.

The experimental setup consists of an amplified laser system (PHAROS, Light Conversion Ltd). The laser has two outputs: one at 800nm ($10\mu J$) and the other at 1445nm ($4\mu J$) with 30 fs and 35 fs pulse durations, respectively. The pulse have a gaussian intensity profile and an approximately TEM_{00} spatial mode. Both these beams are directed to the transient spectrometer where we conduct our pump-probe measurements.

A schematic representation of the transient spectrometer setup that was used is shown in figure 3.1 . In the figure, S1 and S2 represent beam shutters, para1 and para2 represent parabolic mirrors, and BS is a 90:10 beam splitter. The 1445 nm beam is focused onto the the Sapphire crystal to generate a white light super continuum which constitutes the probe beam. We use the 800 nm beam as the pump to excite the sample. The pump and probe beams are focused onto the sample on the same spot with the aid of a Thorlabs CMOS camera to examine the pump-probe overlap (see appendix C). The pump beam after reflection from the sample is blocked. The probe beam is collimated and then, focused onto a narrow ($\approx 20\mu m$) slit at the spectrometer entrance. The spectrometer consists of a grating and a pair of mirrors to direct the individual probe wavelengths onto a 256 channel silicon array detector. The beam intensities were controlled by use of neutral density filters. S1, S2, the chopper and the detector (next to BS) are the main parts of the data acquisition procedure which is presented in the section 3.1.1.

3.1.1 Data acquisition

The signal acquired by the transient spectrometer is already processed,

$$S(\omega,t) = Log\left[\frac{I_{unpumped}(\omega) - I_{dark,unpumped}(\omega)}{I_{pumped}(\omega,t) - I_{dark,pumped}(\omega,t)}\right] \; . \tag{3.1}$$

$I_{unpumped}$ denotes the detector recorded probe intensity when the pump beam is blocked by the chopper and I_{pumped} when the pump beam passes through the chopper. This classification of the recorded probe intensity is obtained using the detector next to the beam splitter. The subscript *dark* represents the background measurement which is obtained using mechanical shutters S1 and S2. The probe beam is blocked by S1 and the spectrometer measures data in the presence of pump (scatter) when S2 is open and also when S2 is closed (electronic noise). The latter corresponds to $I_{dark,pumped}$ and former to $I_{dark,unpumped}$. It should be noted that, even while the background measurement happens, the pump beam continues to be modulated by the chopper. This ensures that the subtracted background takes into account the experimental conditions. There are two measurement settings that decide the number of averages per data point. Number of shots per buffer decide the number of shots that are averaged to give a single data point. A shot is an integration time average of the pumped and unpumped signal. The other setting is number of *buffers per point*. This considers the number of shots per buffer to average over, to obtain a single data point. Modulation of the pump beam during the course of experiment would then be (taking into account that our measurements are reflectivity based, all the measured signal intensity corresponds to reflectivity R),

$$R_{pumped}(\omega, t) = R_{unpumped}(\omega) + \Delta R(\omega, t) \ . \tag{3.2}$$

$\Delta R(\omega, t)$ represents the change in the material reflectivity as a function of probe frequency (ω) and delay time (t). Thus, by suitable changes to equation (**3.1**), taking into account equation (**3.2**), we can get the quantity of interest, the differential reflectivity,

$$\frac{\Delta R(\omega, t)}{R(\omega, t)} = 1 - 10^{-[S(\omega,t)\times 10^3]} \ . \tag{3.3}$$

A factor of 1000 is associated with S as the spectrometer records the data in units of 10^{-3}. R represents the unpumped intensity reflected by the sample. Differential reflectivity quantifies the relative change in reflectivity of the material due to pump perturbation.

3.1.2 Measurement scheme

Our measurements on PbTe were done with a pump average powers of 10 mW (measured before the chopper). The pump beam was at 800 nm and the probe beam was a broad band continuum with a 480 nm-780 nm spectral bandwidth. The focused pump beam on the sample had an angle of incidence of about 5° and the focused probe beam an angle of $\leq 1°$. The measured spot diameters of pump was $d_{pump,a} \approx 73.96\mu m$, $d_{pump,b} \approx 62.32\mu m$ and, that of probe was $d_{probe,a} \approx 29.64\mu m$, $d_{probe,b} \approx 29.05\mu m$ wherein, the subscripts a and b corresponds to the ellipse major and minor axis respectively. The elliptical nature of the laser spot maybe attributed to the incoming angle of the beams, which otherwise have a Gaussian intensity profile. Details on the spot size measurement procedure and the acquired data is presented in Appendix A.3. The measurements were carried out at 25 K, 50 K, 75 K, 100 K, 150 K and 297 K. All of these measurements were made within a cryostat (Oxford) at 2.4×10^{-6}mbar vacuum environment. The detector integration time was set to 0.85 ms, the number of shots per buffer to 300, and number of buffers per point was set to 1. This setting corresponds to a single data point measured over 0.25 s ($= 300 \times 0.85\ ms$). The measurement was broken into three parts, 0-10 ps timescale with a delay stage step size of 0.02 ps per step, 5-50 ps with a step size of 0.5 ps and 5-1000ps with 4 ps.

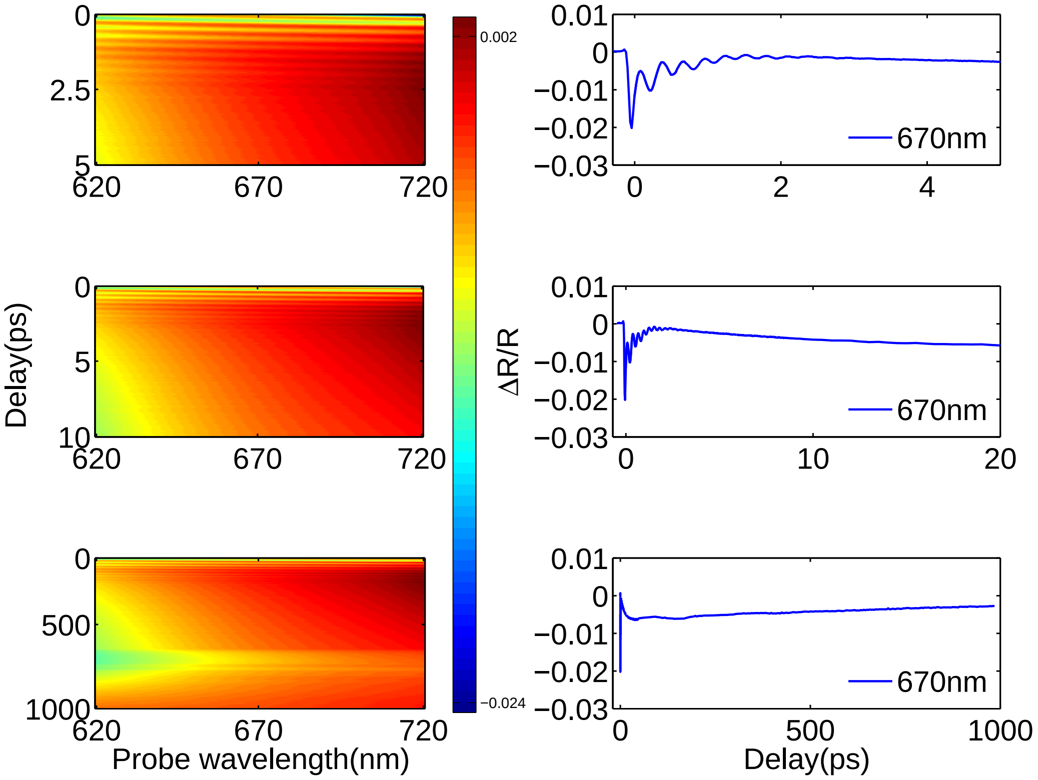

FIGURE 3.2: The $\frac{\Delta R}{R}$ data presented across 620 nm-720 nm at a temperature of 25 K. The data presented here has been broken into 0-5 ps regime (a, b), 0-20 ps (c, d) and 0-1 ns (d, e) regimes to highlight, coherent oscillations, 0-20 ps carrier dynamics and the slow recovery of the system to equillibrium respectively.

3.2 Ultrafast Carrier Dynamics in PbTe

In figure 3.2, we present the raw data between 620 nm-720 nm at 25 K (color plot) and a sample wavelength (670 nm) on three different timescales: 0-5 ps (3.2 (a) and (b)), 0-20 ps (3.2 (c) and (d)), and 0-1 ns (3.2 (e) and (f)). A notable feature of the pump-probe signal is the presence of coherent oscillations (seen as ripples on the color plot) lasting for 4 ps-5 ps (see figures 3.2 (a) and (b)). This is apparent in the 0-10 ps regime and also in the 0-20 ps timescale. Apart from the oscillations, the 0-20 ps data reveal some interesting carrier dynamics. One can notice here a fast response in about a picosecond duration followed by a slow decay on the order of 10's of ps (refer to figures 3.2 (c) and (d)). On considering the full data, up to 1 ns, it can be seen that the system recovers to the initial optical state on an approximately nanosecond timescale (figures 3.2 (e) and (f)) and this is due to carrier diffusion and slow lattice cooling.

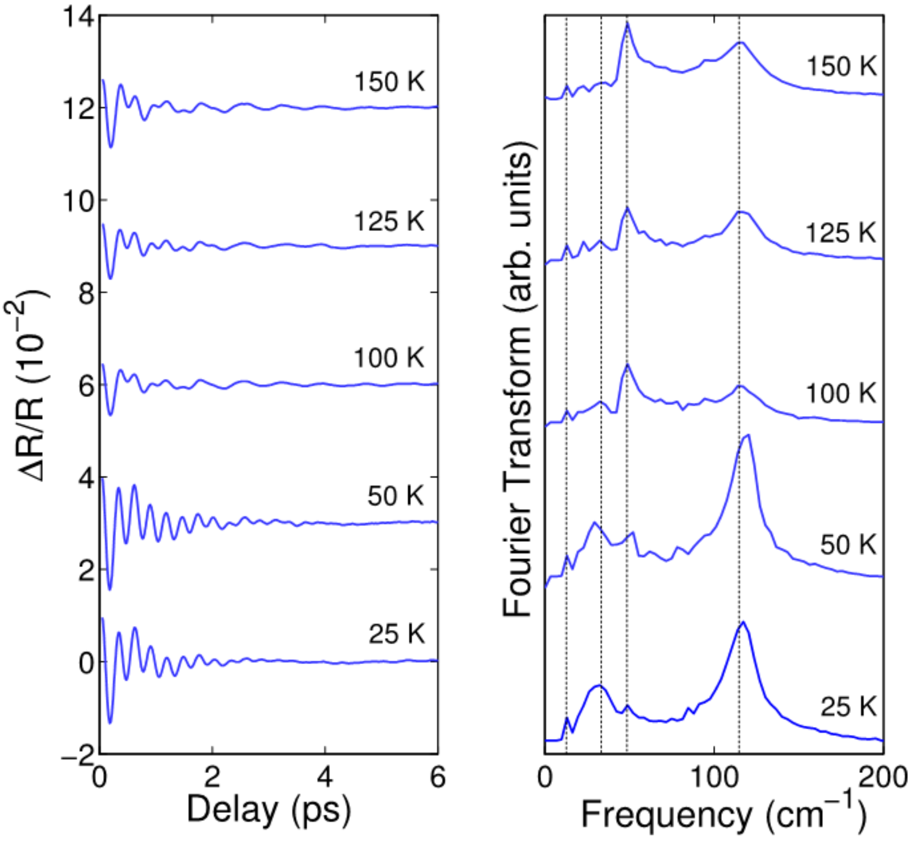

FIGURE 3.3: Coherent oscillations at various measured temperatures and the corresponding component oscillators (obtained from the fast fourier transform of the oscillations). Notice that there are three component oscillators: 113.41 cm^{-1} (3.4 THz), 46.69 cm^{-1} (1.4 THz) and 30.02 cm^{-1} (0.9 THz). Also notice that the magnitude of the individual components are varying across various temperatures.

The coherent oscillations (presented in figure 3.2 (b) and (d)) at first glance may seem to be composed of a single high frequency mode, however, our temperature dependent measurements reveal more detail. In figure 3.3, we can see that the fourier transform of the oscillations in $\Delta R/R$ show peaks at 3.4 THz, 1.4 THz and 0.9 THz. We see that at 25 K and 50 K, the 3.5 THz and the 0.9 THz oscillations have dominant contributions. As we go higher up in temperature, these two modes get damped while the 1.4 THz mode (see 50 K-150 K fourier transform plots, figure 3.3) becomes prominent.

Now we look at the temperature dependence of the carrier dynamics. For the purpose of clarity, we consider the 670 nm data (probe wavelength) on the 0-40 ps time scale. The choice of time scale includes only the relevant carrier dynamics. e^{-}-phonon and phonon-phonon interactions typically happen within the 40 ps duration (see section 2.1.2). Figure 3.4 illustrates the carrier dynamics at different temperatures. Clearly,

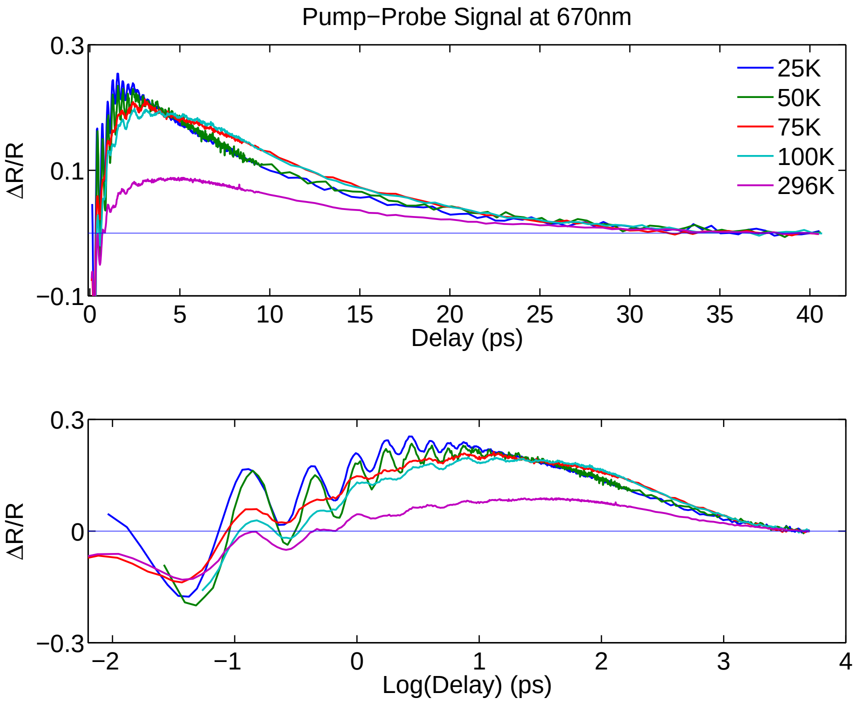

FIGURE 3.4: Pump-probe signal at 670 nm across all the measured temperatures presented on a regular scale and a Log scale. Clearly, the carrier dynamics is differing at different temperatures. The plot presented here has been normalized to 100 K data and the baseline corrected to zero. The Log scale plot is for visualization purposes.

we notice a variation in the carrier lifetimes across various temperatures, particularly between 50 K-75 K. However, it is difficult to deduce the trend in the dynamics on a visual basis.

The detail on the origins of such carrier dynamics and the previously discussed coherent oscillations will be explained in sections that follow. But first, we briefly discuss the data fitting procedure in obtaining the relevant fit parameters, namely, the relaxation time constants and the oscillator decay time constants.

3.2.1 Oscillator data fitting

The raw data in figure 3.2, as discussed earlier, has two major components to it: the coherent oscillations and the carrier dynamics. The fitting problem was addressed in parts; first we fit the oscillators and, then we subtracted this oscillatory background to address the carrier dynamics. To extract the oscillations from the raw data, we considered the 0-10 ps data set. To this data we fit an 8^{th} order *polynomial* to subtract the carrier background. The resultant data then consists of pure oscillations which can be seen in figure 3.5 for the 50 K dataset at 670 nm.

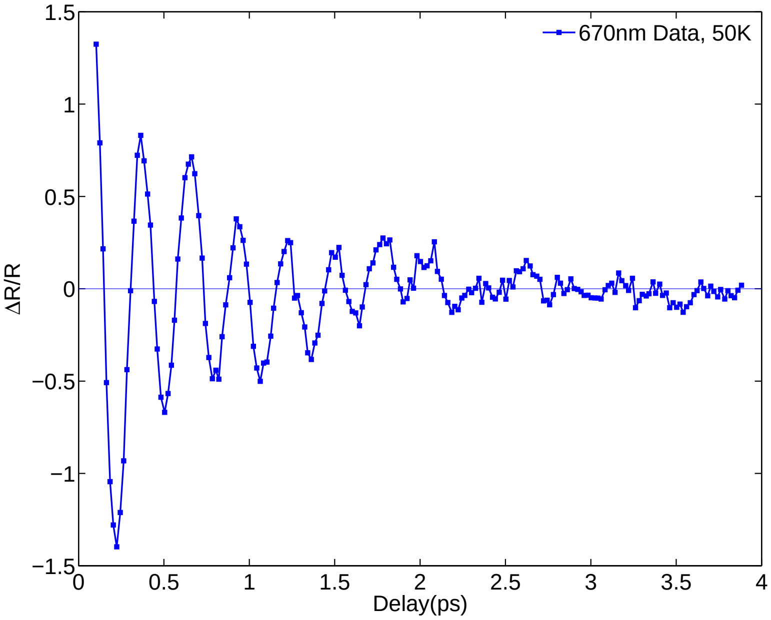

FIGURE 3.5: Pure oscillations extracted from the 50K data at 670nm probe wavelength.

In order to fit these oscillations, we considered the fourier transform of this data to determine the component oscillators. Figure 3.6 shows one such example with the 50 K data set at 670 nm.

In order to fit the oscillations, we used a decaying oscillator model with the frequencies already determined by the peaks in the fourier transform,

$$O(t;\gamma,\beta) = \sum_{i}^{1,2,3} A_i.exp[-t/\gamma_i].sin[\omega_i(t-\beta)] \ . \tag{3.4}$$

In the above fit, ω_i's correspond to previously determined component frequencies multiplied by 2π. γ_i and β represent the fit parameters corresponding to oscillator decay constant and a phase shift term respectively.

The above model was fit to the oscillatory data set using global least squares curve fitting method. This was implemented using a Levenberg-Marquardt algorithm. The least squares method constitutes a minimization problem [15],

$$\frac{\partial S(\Gamma_k)}{\partial \Gamma_k} = \frac{\partial}{\partial \Gamma_k} \sum_i (y_i - f(x_i,\Gamma))^2 = 0 \ . \tag{3.5}$$

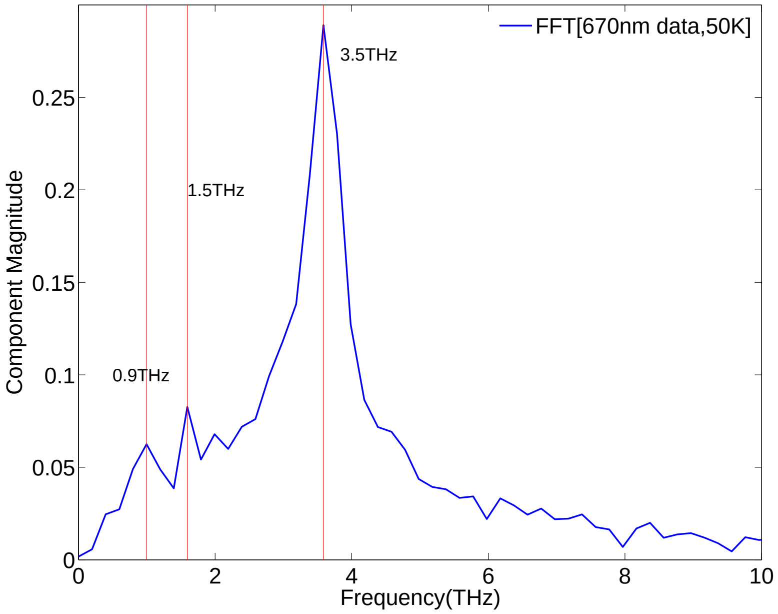

FIGURE 3.6: Fourier space of the time domain data (figure 3.5). The component oscillator peaks have been identified to be 3.5 THz, 1.5 THz and 0.9 THz respectively.

Γ_k are a set of parameters that has to be determined for the data (x_i,y_i) with the model fit function f so that S (residual) is minimized. The Levenberg-Marquardt algorithm approaches this problem by introducing a non-negative *damping factor* (λ) to the least squares problem. The basic idea is to reset λ depending on the rate at which the residual approaches smaller values, at each subsequent iteration. So, smaller rates corresponds to bigger *lambda* and vice versa. Thus, λ damps the deviations from the solution (to solve for Γ_k) and thereby ensures faster convergence [15].

In order to understand the global fit procedure, we need to look at our data set. The pump-probe data was obtained across various probe wavelengths and across 5 different temperatures. Thus, our data sets are parametrized by these two variables. The oscillation dynamics however, are *not* affected by probing wavelength. Thus, the oscillatory part of the data set can be considered to be parametrized by temperature (T) alone. This then means that, it is sufficient to fit a model function of the form in equation (**3.4**) to obtain global parameters across wavelengths, at each temperature (so that $\gamma_i = \gamma_i\ (T)$ and $\beta_i = \beta_i\ (T)$). The details of the global fit implementation can be found in appendix B

3.2.2 Coherent oscillations in PbTe

In section 3.2 we identified the component oscillators to be (figure 3.3) at 3.5 THz, 1.4 THz, and 0.9 THz. In what follows, we first explain the origin of the modes:

1. The 3.5 THz mode can be associated with either of the three possibilities:
    (a) It has been reported that tellurium ions segregate at the surface due to laser induced decomposition of the material in the region being probed [27]. The tellurium surface formed this way has a Raman active phonon mode at approximately 3.5 THz(relevant Raman spectra can be found in [35]). Figure 3.7 shows this observation in Sb_2Te_3. Similar tellurium aggregation are thought to occur in tellurium based compounds.

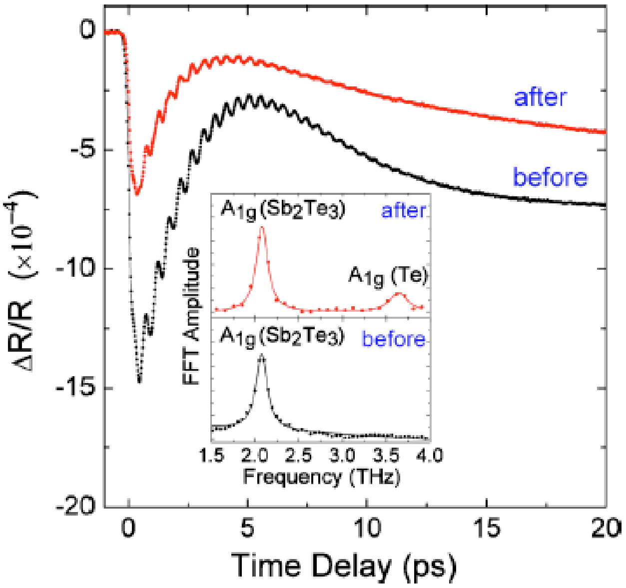

FIGURE 3.7: The appearence of the A_{1g} mode (3.5 THz) due to laser induced decomposition of Sb_2Te_3 [35]. Notice the appearence of the A_{1g} mode *after* laser irradiance (shown in the inset as a fourier transform of the data).

    (b) An interbranch squeezing of the TO and the LA phonon at the X point (TO (X)+LA (X)).
    (c) PbTe has a Raman inactive LO phonon mode at 3.5 THz at the Γ-point which has been observed experimentally by electric field-induced Raman scattering [6].

2. The 1.5 THz mode could be due to interbranch squeezing of the difference mode (TO (X)-LA (X)), which is the counterpart to the mode described in **1**.(**b**).

3. The 0.9 THz mode could be due to the bare TO mode, however, this is not very clear as PbTe is first order Raman inactive. This means, it is not possible to observe coherent phonons at this frequency.

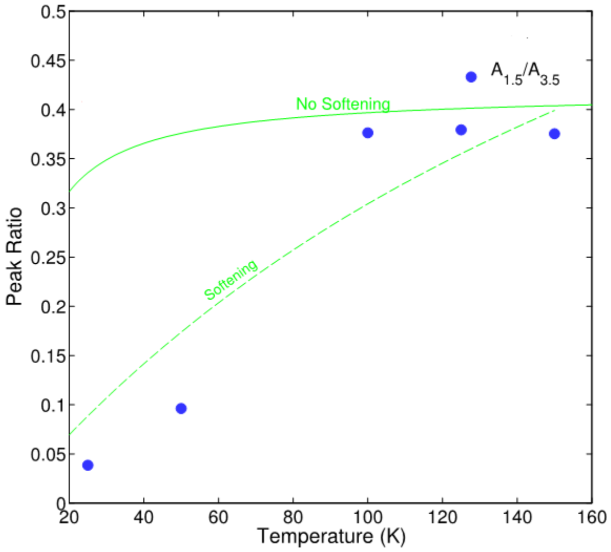

FIGURE 3.8: The ratio of amplitudes of interbranch difference frequency mode (1.5 THz, amplitude $A_{1.5}$) to sum frequency mode (3.5 THz, amplitude $A_{3.5}$). The dashed line and the solid lines are the model fits. The former considers TO mode softening while the latter does not.

As discussed before, PbTe is Raman inactive and it should not be possible to have a LO mode. Moreover, no band bending at the surface occurs in our experiments as no metal-semiconductor junction exists. Thus, this mode is most likely not the LO phonon.

The possibility that the 3.5 THz and the 1.5 THz indeed correspond to interbranch squeezing counterparts can be further investigated by by examining their amplitude versus temperature tendencies. In figure 3.8 we show the ratio of difference mode amplitude ($A_{1.5}$) to the sum mode amplitude ($A_{3.5}$). We can calculate this based on the amplitude behavior of interbranch squeezed modes with temperature, as discussed in section 2.2. From figure 3.8, the solid line represents the calculated amplitude ratio without taking into account TO mode softening. The dashed line considers a 50 percent TO mode softening. The qualitative agreement between the dashed line and the experimental data lends support to our assertion that the 3.5 THz and the 1.5 THz mode are interbranch squeezed state counter parts particularly when we take into account TO mode softening.

3.2.3 Fitting the carrier Dynamics

We now analyze the carrier dynamics by subtracting the oscillatory component using the fit parameters determined in section 3.2.1. For this purpose we consider the data in the 0-40 ps timescale because this choice of time scale includes only the relevant carrier dynamics. As discussed in section 2.1.2, e^{-}-phonon and phonon-phonon interactions typically occur within the 40 ps duration. Figure 3.9 shows an example of the pure carrier dynamics without the oscillatory background for the 670 nm data at 25 K.

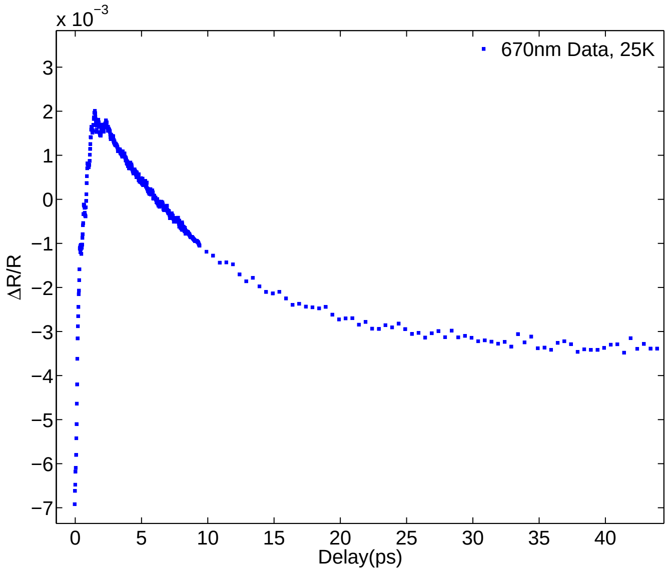

FIGURE 3.9: Pump-probe signal with the oscillatory component subtracted, at 670 nm probe wavelength, 25 K.

In order to fit the carrier dynamics, we use a two decaying exponential model,

$$f(t;\tau,A) = A_0 + A_1.exp[-t/\tau_1] + A_2.exp[-t/\tau_2] \quad . \tag{3.6}$$

A_i and τ_i constitute the fit parameters and correspond to the relaxation time constant and the amplitude of the associated decay channel, respectively. A_0 accounts for the population of long-lived valleys. The curve fitting procedure implemented here is similar to the methods discussed in section 3.2.1. However, we don't consider a global fit here, as the carrier dynamics, in general, depends on the probe wavelength . The variation in the parameters across various wavelengths is small however and is illustrated in figures 3.11-3.12. Figure 3.10 shows the model fit for 670 nm, at 25 K as an example.

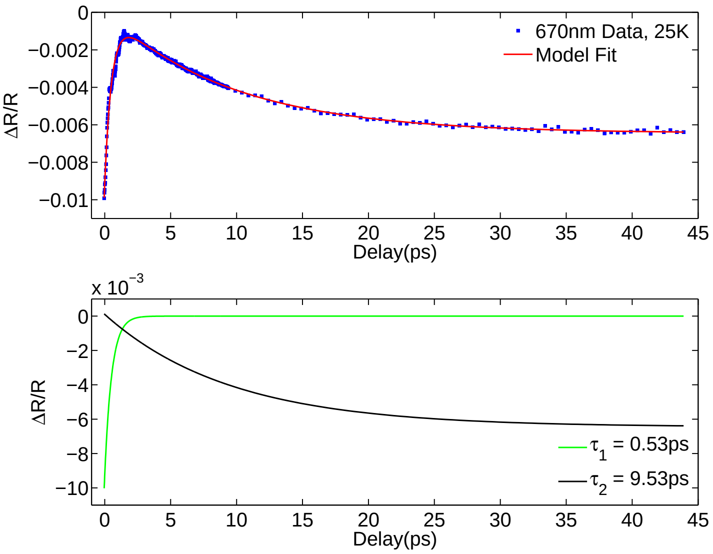

FIGURE 3.10: Model fit for the 670nm, 25K data. The fit function components have decay constants of 0.53 ps and 9.53 ps.

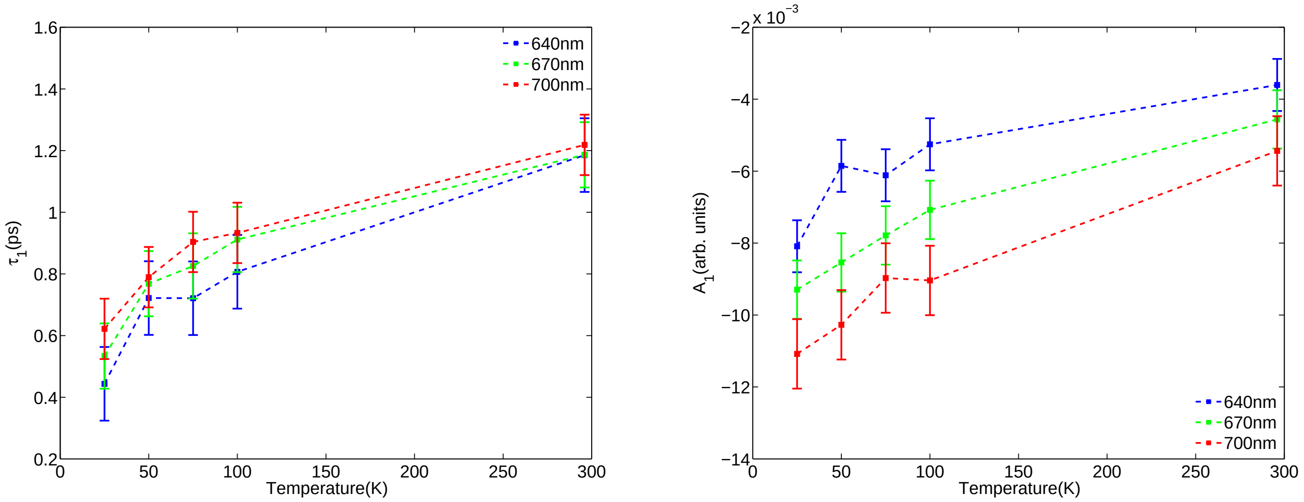

FIGURE 3.11: Left: The fast relaxation decay component as a function of temperature and wavelength. The trend is an increasing one and the parameter ranges between 0.4 ps-1.2 ps. Right: The amplitude (A_1) for the fast decay channel seems to be negative and increasing with temperature.

3.2.4 Carrier dynamics in PbTe

From figure 3.11 we notice that the relaxation time (τ_1) increases with temperature. The range of τ_1 (0.4 ps-1.2 ps) is consistent with the time scale of e^--optical phonon interaction (see section 2.1.2). These include e^--TO and e^--LO interactions. We can combine our discussions from sections 2.1.3 and 2.1.4 to qualitatively describe the observed τ_1:

1. The e^--TO interaction Hamiltonian ($\mathcal{H}_{TO}$) has an inverse proportionality to the TO mode frequency (ω_{TO}),
$$\mathcal{H}_{TO} \propto \sqrt{\frac{1}{\omega_{TO}}} \ . \tag{3.7}$$

2. The TO mode softens at the zone center,
$$\omega_{TO}^2 \left(q \approx 0\right) \propto \left(T - T_c\right) \ . \tag{3.8}$$

3. Combining **1**. and **2**., we have the following temperature dependency for $\mathcal{H}_{LO}$,
$$\mathcal{H}_{TO} \propto \sqrt{\frac{1}{T - T_c}} \tag{3.9}$$
This would mean that at low temperatures, the e^--TO interaction becomes strong.

4. Based on laser fluence calculation, we determined the laser induced carrier density to be on the order of 10^{20} (see appendix C), three orders of magnitude larger than the intrinsic carrier density. It is known that, under sufficiently large carrier densities, Fr*ö*hlich interactions can be partially screened resulting in a weaker e^--LO interaction [26] [48]. Qualitatively, screening refers to the fact that, when there are sufficient carrier densities, these excess carriers can screen the longitudnal **E**-field of the LO mode. This partially reduces the intensity of the interaction field. Thus, we assume a partial screening of the LO mode interaction. This makes e^--TO scattering the dominant relaxation mechanism on this time scale.

From points (**1**.)-(**5**.) we can conclude qualitatively that these arguments can account for the observed increase in τ_1. It should be noted that the TO (LO) mode interaction (through the deformation potential) in semiconductors (with zinc blende crystal structure) with a direct band gap at the Γ such as GaAs is forbidden due to selection rules [r]; the symmetries of the state at Γ (s-like) and that of the interaction Hamiltonian do not permit intraband transitions between non-degenerate states in the conduction band by the emission of TO phonons. However, this is *not* the case with PbTe as it has a band gap at the L-point and the state symmetry (p-like [40]) permits intraband transitions by interactions with TO modes through deformation potential interaction.

Theoretical calculations to understand the behaviour of τ_1 as a function of temperature due to e^{-}-optical phonon deformation potential interaction exist [14],

$$\tau_1 \propto T^{\frac{-3}{2}} \Xi^{-2} \quad . \tag{3.10}$$

Here Ξ corresponds to the deformation potential. This can be explained by the fact that, the temperature dependence appearing in equation (**3.10**) comes from the evaluation of,

$$|\langle \mathbf{k}^{'}, n^{'}_{\mathbf{q}} | \mathcal{H}_{e^{-}-LA} | \mathbf{k}, n_{\mathbf{q}} \rangle|^2 \quad , \tag{3.11}$$

where $n^{'}_{\mathbf{q}}$ and $n_{\mathbf{q}}$ corresponds to the phonon initial and final occupation numbers, respectively. $\mathbf{k}^{'}$ and $\mathbf{k}$ corresponds to the final and initial momentum states of the electron. The temperature dependence is due to the evaluation of $n_{\mathbf{q}} \approx n_{\mathbf{q}} + 1 \approx \frac{k_B T}{\hbar \omega_q}$. This approximation however is only valid for $\hbar\omega_q << k_B T$, which is not the case for low temperatures, where we observe the peculiar behavior for the fast and slow relaxation time. Additionally, it should be noted that these calculations do not take into account TO mode softening or the temperature dependence of Ξ. Moreover, it has been found that, Ξ shows an increase with increasing temperature [49]. However, deformation potentials can be difficult to calculate, hard to determine experimentally, and there exists large discrepancies in the calculated and experimental values [49].

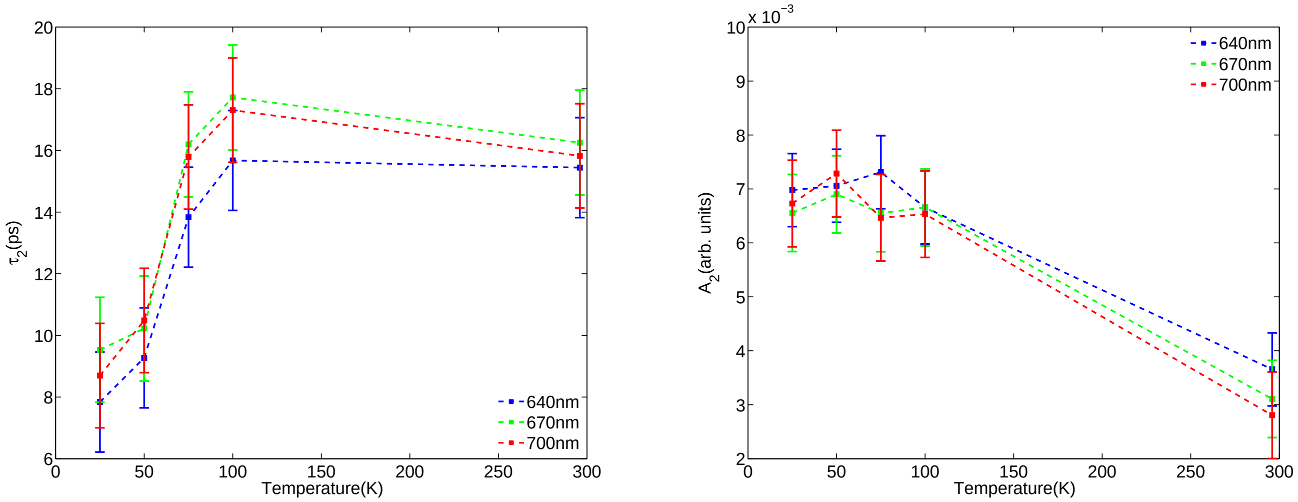

FIGURE 3.12: Left: The slow relaxation decay component as a function of temperature and wavelength. The trend is an increasing one and the parameter ranges between 8 ps-18 ps. Right: The amplitude (α_2) for the fast decay channel seems to be positive and decreasing with temperature.

In figure 3.12 the time range for the τ_2 (8 ps-18 ps) is consistent with two possibilities: e^--acoustic phonon interactions and optical phonon-acoustic phonon interactions (2.1.2). Further, we see a dramatic dip in τ_2 at $\approx$ 100 K, and we must see if these two relaxation mechanisms can explain this. We will begin by considering the e^--acoustic phonon interactions. Based on discussions in section 2.1.3 we have:

1. The deformation potential associated with TA mode is generally lower than that associated with LA mode due to the nature of the modes. This fact can be qualitatively understood based on the fact that the LA mode constitute shear *and* volume changes to the lattice. The TA mode however, constitutes only a shearing of the lattice. This would mean that, in terms of lattice deformation, the LA mode has larger deformation potential than the TA mode and contributes more to the relaxation on these timescales.
2. The interaction Hamiltonian ($\mathcal{H}_{LA}$) for e^--LA phonon interaction depends on the mode frequency ω_{LA} as,
$$\mathcal{H}_{LA} \propto \sqrt{\frac{1}{\omega_{LA}}} \; . \tag{3.12}$$
3. We have seen that the TO mode softens with temperature. From our discussions in section 2.3 , we notice that TO mode softens the LA mode, additionally due to strong anharmonic coupling between TO and LA mode.
4. From the above arguments, we can see that on a qualitative basis, the interaction strength should increase with decreasing temperature, as we see in figure 3.12 for the 10-100 K range. The explicit functional form for LA mode softening is not known, however.

Thus, the e^--LA interaction is the dominant e^--phonon interaction consistent with the smaller τ_2 with decreasing temperature.

Now we consider the case of optical phonon-acoustic phonon interactions:

1. TO-LA interactions are strong in PbTe due to the anharmonic coupling between these modes (see the discussion in section 2.3). Since we have seen that the TO mode softens with temperature, it is possible that the TO-LA interaction gets stronger with decreasing temperature.
2. Stronger e^--TO interactions as opposed to e^--LO interactions (due to screening effects as discussed earlier) result in greater population for the TO mode phonons in comparison to LO mode phonons. Consequently, the TO-acoustic mode interaction channel dominates the LO-acoustic mode interactions. As far as TO-TA

> interactions are concerned, they do exist but, these are not as prominent as TO-LA. This is attributed to the particularly strong coupling between these modes.

Thus, the TO-LA interaction constitutes the dominant optical phonon-acoustic phonon interaction. This means, from the above discussion, that τ_2 should become smaller with decrease in temperature.

From the above discussion we can infer that, *both* e^--acoustic phonon *and* optical phonon-acoustic phonon interactions qualitatively explain the observed trend. This implies that, the contribution to τ_2 is a mixture of both types of interactions, and the temperature sensitivity of both the channels may account for the more pronounced temperature dependence.

Chapter 4

Conclusion and Outlook

During the course of this thesis we understood that lead telluride has some unexpected characteristics which are contradictory to those observed in most semiconductors with similar structure. Notable amongst these peculiarities was the band gap behavior with temperature. It increases with temperature and this is not the case with most semiconductors which show an opposite trend, such as Si for example. These peculiarities extend to the observed low thermal conductivity in PbTe as well. From recent inelastic neutron scattering studies on PbTe [13], we understood that strong phonon-phonon (TO-LA) interactions can be responsible for the observed low lattice thermal conductivity. These studies motivated us to further investigate the dynamics of these interactions. We observed, based on ultrafast techniques, some unexpected trends in the electron-phonon and phonon-phonon relaxation times. We saw that, the interaction time constants associated with electron-phonon and phonon-phonon interactions decrease with temperature. This is contradictory to theoretical calculations for these materials (lead chalcogenides). However, we also noticed that these calculations don't take into account TO and LA mode softening behavior. Moreover, we realized that only possible way to exaplain the observed trends is by considering mode softening and the anharmonic coupling of the TO and LA modes. Thus, in the process of understanding carrier dynamics, we obtained data consistent with the conclusions of Delaire, et.al.

Coherent oscillations were also part of the observation in our experiment. We deduced that these oscillations are a combination of three oscillator modes, 3.5 THz, 1.5 THz, and 0.9 THz. Also, the 0.9 THz mode becomes prominent with increasing temperature and 1.5 THz and 3.5 THz modes become less important. We were able to explain the behavior of the high frequency modes on the basis of interbranch squeezing at the X-point resulting in squeezed phonons. The behavior of 0.9 THz mode, however, still remains elusive and needs further investigation.

In this project we studied the temperature behavior of TO+LA modes on a time domain basis. The next approach would be to supplement the observations with temperature dependent spontaneous Raman measurements which is a direct method of studying phonon modes. This will also help to understand the TO mode softening with temperature due to flat dispersion relation and the sharp density of states peak at the Γ-point. Our current measurements lacks carrier dynamics behavior between 100 K and room temperature. Thus, next step would be to include temperature sensitive carrier dynamics studies in those temperature range. In this thesis, we qualitatively accounted for the carrier dynamics. So, it would be appropriate to model these dynamics with three temperature model to account for multiple subsystem that exchange energy in this material.

Appendices

Appendix A

Temporal resolution in a pump-probe experiment

As discussed earlier in Chapter 1, the temporal resolution in a pump-probe experiment mostly boils down to pulse width. To be more specific, the pump-probe cross correlation pulse width. To illustrate this, we consider a simple case of semiconductors. We start by assuming an instantaneous system response R(t) to pump excitation and, the decay dynamics to have an exponential dependence (with pump-probe delay time t as the parameter), as the functional form(typical of most semiconductor materials, for example, GaAs):

$$R(t) = \theta(t). \sum_{i}^{e-e,e-ph,ph-ph...} (A_i.exp[-t/\tau_i]) \tag{A.1}$$

$\theta(t)$ corresponds to an unit step function with $\theta(t) = 0$ for $t < 0$ and $\theta(t) = 1$ for $t \geq 1$ picosecond(ps) highlighting our assumpition of instantaneous system response. The summation is over various scattering mechanisms in a semiconductor material as discussed in sections 2.1.2 and 2.1.4 . Because the energy delivered by the pump(p(t)) beam is not instantaneous, but over a a pulse width duration(σ), the observed system response would be a convolution of p(t) and R(t), G(t):

$$G(t) = \int_{-\infty}^{\infty} dt^{'} R(t).p(t^{'} - t) \tag{A.2}$$

Probing with finite pulse width would then imply a second convolution of probe pulse form(pr(t), pulse width σ) with G(t), so that the observed signal would be $\widetilde{G}(t)$:

$$\widetilde{G}(t) = \int_{-\infty}^{\infty} dt^{'} G(t).pr(t^{'} - t) \tag{A.3}$$

This upon appropriate simplification would yield, for gaussian pulse shape:

$$\widetilde{G}(t) = \sum_{i}^{e-e,e-ph,ph-ph...} \alpha_i \left[exp[-t/\tau_i].[1 + erf\left(\frac{\sqrt{2}\sigma}{2\tau_i} - \frac{t}{\sqrt{2}\sigma}\right)] \right] \tag{A.4}$$

$\widetilde{G}(t)$ represents the pump-probe signal as a function of time. Figure A.1 represents the system response for different values of pump-probe cross correlation pulse width divided by $\sqrt{2}$ (σ). And, in the figure, $\widetilde{G(t)} = C(t) * R(t)$ where C(t) is the pump-probe cross correlation function which is a way of representing $\widetilde{G(t)}$:

$$\widetilde{G(t)} = pr(t) * \underbrace{(p(t) * R(t))}_{G(t)} = \underbrace{(pr(t) * p(t))}_{C(t)} * R(t) \tag{A.5}$$

Where * represents convolution of functions. For the purpose of illustration, we have assumed a two exponential component in equation(**A.1**) and considered one of the components to have a time constant of 1 ps and the other to be 10 ps. We consider 3 different values of pump-probe pulse width 0.1 ps, 1 ps, 10 ps.

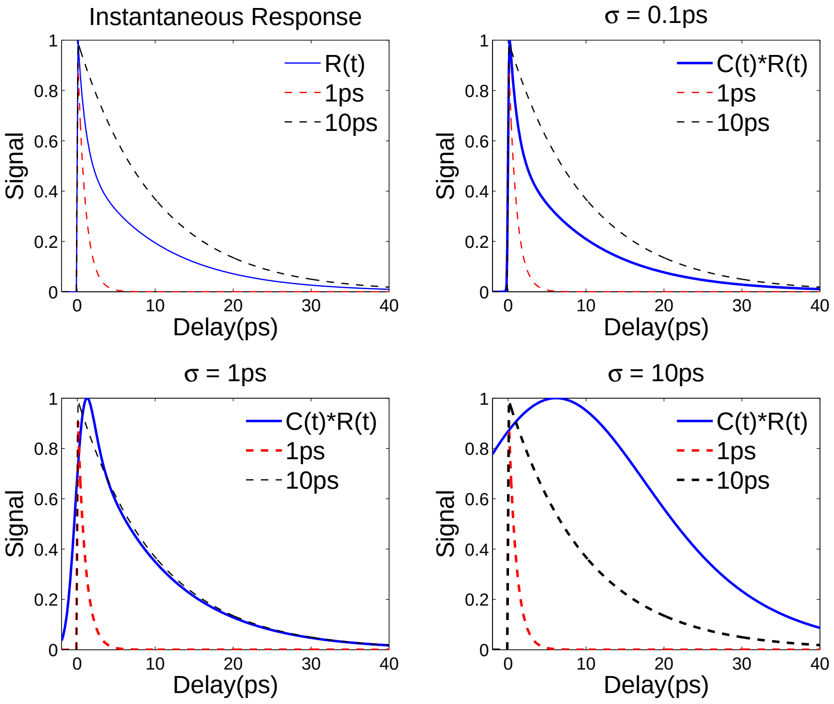

Figure A.1: Left to right(top): System response plotted along with the component decay channels(left). The system response as measured for a $\sigma = 0.1$ ps. Notice the close resemblance between actual response and the pulse stimulated response; all the decay components are well resolved(right). Left to right(bottom): The system fast response is mostly unresolved at $\sigma = 1$ ps(left). For $\sigma = 10$ ps, the 1 ps components is completely obscured while 10ps component is mostly unresolved(right). Comparing with instantaneous response would reveal these distinctions better.

Appendix B

Global fit algorithm for coherent oscillations

Contents

- Curve fitting:
- GLOBAL FIT TO DETERMINE THE DECAY PARAMETERS @25K:

```
R25K = importdata( 'E:\Academics\Course work\3rd Semester\Master The
T25K = importdata( 'E:\Academics\Course work\3rd Semester\Master The
```

Curve fitting:

```
b = 7;
c = [1 0.3 1 0.3 0.3 3 3 4 5 3 3];
for i = 11:11;
% x0 = [-3; c(i); 0.5; 1; -1; 0.1; 0.04];
% opts=optimset('TolFun',1e-12,'MaxIter',6000,'TolX',1e-12,'Algorit
% [x,output,~,exitflag,resnorm,xfinal] = lsqcurvefit(@Oscillator,x0
% plot(T25K([b:end],i),R25K([b:end],i)+2*i,T25K([b:end],i),Oscillat
% exitflag
% scatter(i,exitflag)
% scatter(i,x(2))
% scatter(i,x(5))
% scatter(i,x(7))
% hold on;

%To check if the oscillators are color dependent:
% plot(T25K([b:end],i),R25K([b:end],i)+0.5*i)
% hold on;
end
```

GLOBAL FIT TO DETERMINE THE DECAY PARAMETERS @25K:

```
q = 194;
Oscn25globLR = vertcat(R25K([b:end],1),R25K([b:end],2),R25K([b:end]
Oscn25globLT = vertcat(T25K([b:end],1),T25K([b:end],2),T25K([b:end]
Label25K = vertcat(1*ones(q,1),2*ones(q,1),3*ones(q,1),4*ones(q,1),
Timevector25K = [Oscn25globLT Label25K];

O0 = [-3*ones(1,11) 2 0.5*ones(1,11) 1*ones(1,11) 1 0.1*ones(1,11)
opts=optimset('TolFun',1e-12,'MaxIter',6000,'TolX',1e-12,'Algorith
[O25K,output,~,exitflag,resnorm,xfinal] = lsqcurvefit(@Oscillator,O
for i = 1:3:11
plot(T25K([b:end],i),R25K([b:end],i)+2*i)
hold on;
plot(T25K([b:end],i),O25K(i).*exp(-(T25K([b:end],i))/O25K(12)).*sin
hold on;
```

FIGURE B.1: The Global fit algorithm.

Appendix C

Spot size measurement and carrier density estimation

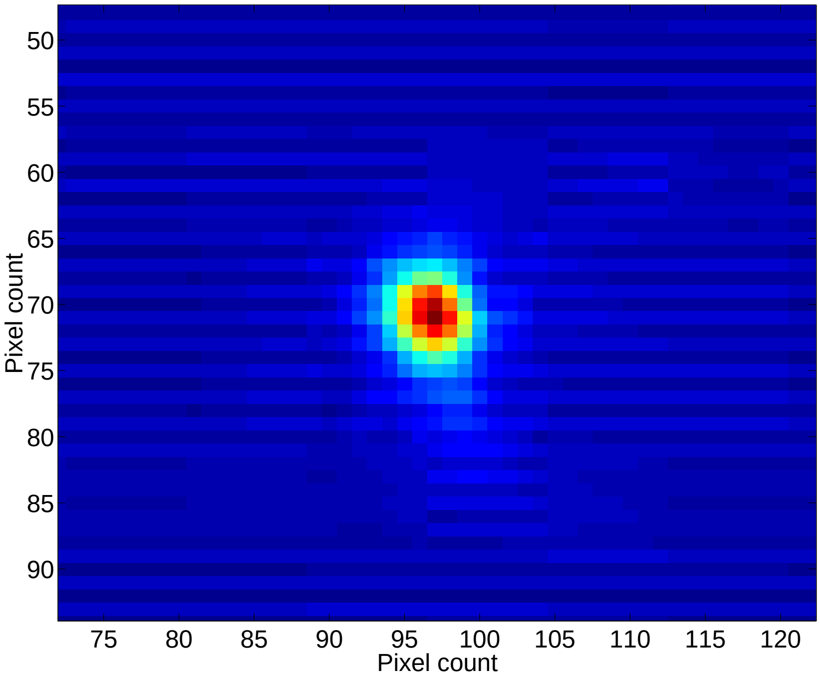

Figure C.1: Probe beam profile with $d_{probe,a} \approx 29.64\ \mu m$ and $d_{probe,b} \approx 29.05\ \mu m$

The spot size measurement was done with a THORLABS DCC1545M CMOS camera (1 pixel $\approx 5.2\ \mu m^2$) with the use of neutral density filters (to prevent detector saturation

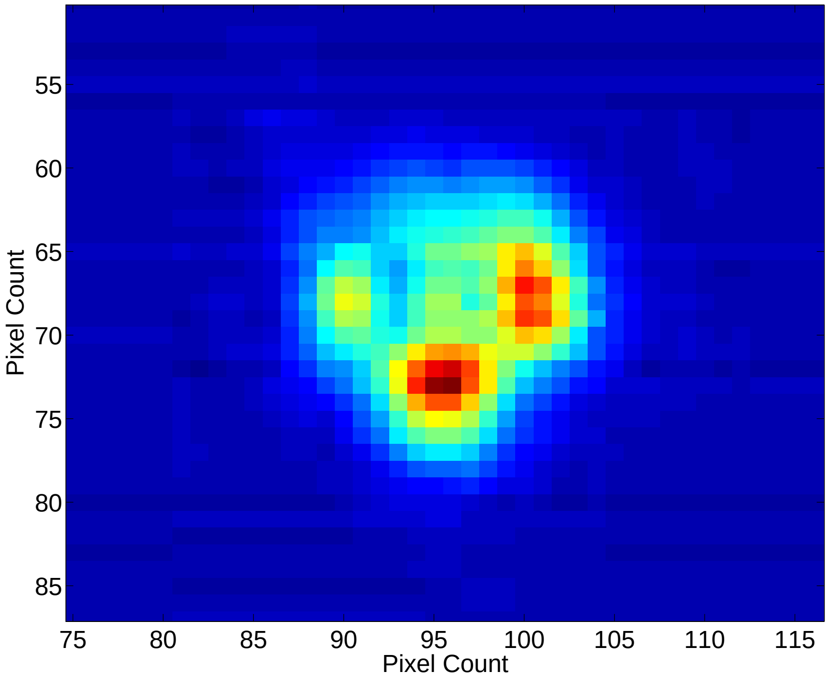

FIGURE C.2: Pump beam profile with $d_{pump,a} \approx 73.96\ \mu m$ and $d_{pump,b} \approx 62.32\ \mu m$

and damage). The positioning of the camera was as close to the actual sample configuration during the course of pump-probe experiment. In order to calculate the effective carrier density excited by the pump(N_c), we calculate the effective pump-fluence first [37] :

$$f_{eff} = f_c\left(\left[1+\left(\frac{w_x}{w_0}\right)^2\right]\left[1+\left(\frac{w_y}{w_0}\right)^2\right]\right)^{-\frac{1}{2}} \tag{C.1}$$

where f_c(1.927 Jcm^{-2}) represents the normal incidence pump fluence(this assumption is strictly not valid in our case as the pump is incident at an angle, however, this can be used for a rough estimate). w_x and w_y corresponds to half of the minor and major axis dimensions of the probe spot(14.82 μm and 14.53 μm). w_0 is the pump beam radii(68.14 μm). The calculated f_c then corresponds to 1.6 mJcm^{-2}. This is then used to calculate N_c [37] :

$$N_c = (1-R_n)f_{eff}\left(\frac{\alpha}{E_{ph}}\right) \tag{C.2}$$

Here, R_n corresponds to pump normal incidence reflectivity(assumed value:), and

E_{ph} the photon energy at the central pump wavelength(at 800 nm, 2.48×10^{-19} J). α corresponds to the absorption coefficient of the material at this pump wavelength. This gives the carrier density at the surface of the material. On assuming a exponential decay dependence for the absorbed pump radiation, we can estimate the total carrier density:

$$N_{total} = \frac{w_0^2}{\delta} \int_0^{\delta} dz.exp(-\alpha z)N_c \tag{C.3}$$

so that, N_{total} corresponds to 2.1×10^{20} at 300 K and 2.9×10^{20} at 5 K. Here, δ is the penetration depth at 800 nm and we have assumed the absorption to happen in a cylindrical volume of depth δ.

Bibliography

[1] H.A. Alperin, S.J. Pickart, J.J. Rhyne, and V.J. Minkiewicz. Softening of the transverse-optic mode in pbte. *Physics Letters A*, 40(4):295 – 296, 1972. ISSN 0375-9601. doi: http://dx.doi.org/10.1016/0375-9601(72)90578-6. URL http://www.sciencedirect.com/science/article/pii/0375960172905786.

[2] J Antoinette and P Rohit. *Optical Techniques for Solid-State Materials Characterization*. ISBN 9781439814376.

[3] Neil W. Ashcroft and N. David Mermin. (Solid State Physics) Neil W. Ashcroft, N. David Mermin-Brooks Cole (1976).

[4] Á. Bardócz. Device for high-precision time-resolved spectroscopy. *Spectrochim. Acta*, 16(1953):1173–IN2, 1960. ISSN 03711951. doi: 10.1016/0371-1951(60)80222-6.

[5] R. T. Bate, D. L. Carter, and J. S. Wrobel. Paraelectric behavior of pbte. *Phys. Rev. Lett.*, 25:159–162, Jul 1970. doi: 10.1103/PhysRevLett.25.159. URL http://link.aps.org/doi/10.1103/PhysRevLett.25.159.

[6] L. Brillson and E. Burstein. Surface electric-field¯induced raman scattering in pbte and snte. *Phys. Rev. Lett.*, 27:808–811, Sep 1971. doi: 10.1103/PhysRevLett.27.808. URL http://link.aps.org/doi/10.1103/PhysRevLett.27.808.

[7] Manuel Cardona and D. L. Greenaway. Optical properties and band structure of group IV-VI and group V materials. *Phys. Rev.*, 133(6A), 1964. ISSN 0031899X. doi: 10.1103/PhysRev.133.A1685.

[8] J. K. Chen, D. Y. Tzou, and J. E. Beraun. A semiclassical two-temperature model for ultrafast laser heating. *Int. J. Heat Mass Transf.*, 49(1-2):307–316, 2006. ISSN 00179310. doi: 10.1016/j.ijheatmasstransfer.2005.06.022.

[9] W. Cochran. Crystal stability and the theory of ferroelectricity. *Phys. Rev. Lett.*, 3:412–414, Nov 1959. doi: 10.1103/PhysRevLett.3.412. URL http://link.aps.org/doi/10.1103/PhysRevLett.3.412.

[10] W. Cochran. The crystal dynamics of lead telluride. *...R. ...*, 293: 433–451, 1966. ISSN 1364-5021. doi: 10.1098/rspa.1966.0182. URL `http://rspa.royalsocietypublishing.org/cgi/doi/10.1098/rspa.1966.0182$\delimiter"026E30F$nhttp://rspa.royalsocietypublishing.org/content/293/1435/433.short`.

[11] P. B. Corkum. Attosecond science. *Springer Ser. Opt. Sci.*, 177:3–7, 2013. ISSN 03424111. doi: 10.1007/978-3-642-37623-8-1.

[12] Richard Dalven. A review of the semiconductor properties of PbTe, PbSe, PbS and PbO. *Infrared Phys.*, 9(4):141–184, December 1969. ISSN 00200891. doi: 10.1016/0020-0891(69)90022-0. URL `http://linkinghub.elsevier.com/retrieve/pii/0020089169900220`.

[13] O Delaire, J Ma, K Marty, a F May, M a McGuire, M-H Du, D J Singh, a Podlesnyak, G Ehlers, M D Lumsden, and B C Sales. Giant anharmonic phonon scattering in PbTe. *Nat. Mater.*, 10(8):614–619, 2011. ISSN 1476-1122. doi: 10.1038/nmat3035. URL `http://dx.doi.org/10.1038/nmat3035`.

[14] Koumoto et.al (Eds.). Thermoelectric Nanomaterials Materials Design and Applications.

[15] Curve fitting. Levenberg Marquardt. `http://en.wikipedia.org/wiki/Levenberg-Marquardt_algorithm`.

[16] John T. Foley and Uzi Landman. Model dielectric function for semiconductors: Si. *Phys. Rev. B*, 14(4):1597–1604, 1976. ISSN 01631829. doi: 10.1103/PhysRevB.14.1597.

[17] Mark Fox. (Oxford master series in condensed matter physics) Mark Fox-Optical properties of solids-Oxford University Press (2001).

[18] J L Hunt. of Physics. (1962), 1976.

[19] Evan O. Kane. Strain effects on optical critical-point structure in diamond-type crystals. *Phys. Rev.*, 178(3):1368–1398, 1969. ISSN 0031899X. doi: 10.1103/PhysRev.178.1368.

[20] Charles Keffer, Timothy M. Hayes, and Arthur Bienenstock. Debye-Waller factors and the PbTe band-gap temperature dependence. *Phys. Rev. B*, 2(6):1966–1976, 1970. ISSN 01631829. doi: 10.1103/PhysRevB.2.1966.

[21] Charles Kim, J. Garland, and P. Raccah. Modeling the optical dielectric function of the alloy system AlxGa1-xAs. *Phys. Rev. B*, 47(4):1876–1888, 1993. ISSN 0163-1829. doi: 10.1103/PhysRevB.47.1876.

[22] Andrei Kirilyuk, Alexey V. Kimel, and Theo Rasing. Ultrafast optical manipulation of magnetic order. *Rev. Mod. Phys.*, 82(3):2731–2784, September 2010. ISSN 0034-6861. doi: 10.1103/RevModPhys.82.2731. URL `http://link.aps.org/doi/10.1103/RevModPhys.82.2731`.

[23] S. E. Kohn, P. Y. Yu, Y. Petroff, Y. R. Shen, Y. Tsang, and M. L. Cohen. Electronic band structure and optical properties of PbTe, PbSe, and PbS. *Phys. Rev. B*, 8(4): 1477–1488, 1973. ISSN 01631829. doi: 10.1103/PhysRevB.8.1477.

[24] Yi-ping Lai, Hsueh-ju Chen, Kuang-hsiung Wu, and Jia-ming Liu. Temperature-dependent carrier – phonon coupling in topological insulator. 232110(2014), 2014. doi: 10.1063/1.4904009.

[25] Aaron D. Lalonde, Yanzhong Pei, Heng Wang, and G. Jeffrey Snyder. Lead telluride alloy thermoelectrics. *Mater. Today*, 14(11):526–532, 2011. ISSN 13697021. doi: 10.1016/S1369-7021(11)70278-4. URL `http://dx.doi.org/10.1016/S1369-7021(11)70278-4`.

[26] R.F. Leheny, Jagdeep Shah, R.L. Fork, C.V. Shank, and a. Migus. Dynamics of hot carrier cooling in photo-excited GaAs. *Solid State Commun.*, 31(11):809–813, 1979. ISSN 00381098. doi: 10.1016/0038-1098(79)90393-4.

[27] Yuwei Li, Vladimir a Stoica, Lynn Endicott, Guoyu Wang, and Ctirad Uher. Coherent optical phonon spectroscopy studies of femtosecond-laser modified Sb2Te3 films Coherent optical phonon spectroscopy studies of femtosecond-laser modified Sb 2 Te 3 films. *Appl. Phys. Lett.*, 97(2010):171908–3, 2010. ISSN 00036951. doi: 10.1063/1.3499742.

[28] C.J. Milne, T.J. Penfold, and M. Chergui. Recent experimental and theoretical developments in time-resolved X-ray spectroscopies. *Coord. Chem. Rev.*, 277-278 (February):44–68, 2014. ISSN 00108545. doi: 10.1016/j.ccr.2014.02.013. URL `http://www.sciencedirect.com/science/article/pii/S0010854514000630`.

[29] K. P. O'Donnell and X. Chen. Temperature dependence of semiconductor band gaps. *Appl. Phys. Lett.*, 58(25):2924–2926, 1991. ISSN 00036951. doi: 10.1063/1.104723.

[30] D. Olguín, M. Cardona, and a. Cantarero. Electron-phonon effects on the direct band gap in semiconductors: LCAO calculations. *Solid State Commun.*, 122(11): 575–589, 2002. ISSN 00381098. doi: 10.1016/S0038-1098(02)00225-9.

[31] Andreas Othonos. Probing ultrafast carrier and phonon dynamics in semiconductors. *J. Appl. Phys.*, 83(4):1789, 1998. ISSN 00218979. doi: 10.1063/

1.367411. URL `http://scitation.aip.org/content/aip/journal/jap/83/4/10.1063/1.367411`.

[32] PbTe. FCC, Brillouin zonel. `http://cmt.dur.ac.uk/sjc/thesis_dbj/node75.html`,.

[33] PbTe. direct Lattice. `http://upload.wikimedia.org/wikipedia/commons/c/c0/NaCl_polyhedra.png`,.

[34] Yu Peter and M Cardona. *Fundamentals of Semiconductors Physics and Materials Properties*. ISBN 9783642007095.

[35] A. S. Pine and G. Dresselhaus. Raman spectra and lattice dynamics of tellurium. *Phys. Rev. B*, 4:356–371, Jul 1971. doi: 10.1103/PhysRevB.4.356. URL `http://link.aps.org/doi/10.1103/PhysRevB.4.356`.

[36] Fausto Rossi. Theory of ultrafast phenomena in photoexcited semiconductors. 74 (July):895–950, 2002.

[37] a. Sabbah and D. Riffe. Femtosecond pump-probe reflectivity study of silicon carrier dynamics. *Phys. Rev. B*, 66(16):1–11, 2002. ISSN 0163-1829. doi: 10.1103/PhysRevB.66.165217.

[38] Marvin E L A S See and Henry Lkvinstein. Properties of Lead Telluride*. 175 (1953):2–7, 1954.

[39] G Jeffrey Snyder and Eric S Toberer. Complex thermoelectric materials. *Nat. Mater.*, 7(February):105–114, 2008. ISSN 1476-1122. doi: 10.1038/nmat2090.

[40] FengQing Sun. Ultrafast transient absorption study of lead-salt colloidal quantum dots carrier dynamics. `http://search.proquest.com/docview/304661414`.

[41] Yasuhiko Terada, Masahiro Aoyama, Hiroyuki Kondo, Atsushi Taninaka, Osamu Takeuchi, and Hidemi Shigekawa. Ultrafast photoinduced carrier dynamics in GaNAs probed using femtosecond time-resolved scanning tunnelling microscopy. *Nanotechnology*, 18:044028, 2006. ISSN 0957-4484. doi: 10.1088/0957-4484/18/4/044028.

[42] Yasuhiko Terada, Shoji Yoshida, Osamu Takeuchi, and Hidemi Shigekawa. Real-space imaging of transient carrier dynamics by nanoscale pump–probe microscopy. *Nat. Photonics*, 4(12):869–874, October 2010. ISSN 1749-4885. doi: 10.1038/nphoton.2010.235. URL `http://www.nature.com/doifinder/10.1038/nphoton.2010.235`.

[43] John W. G. Tisch. Attosecond physics: Ultrafast goes ultralong. *Nat. Phys.*, 4(May): 350–351, 2008. ISSN 1745-2473. doi: 10.1038/nphys957.

[44] Terry M Tritt and M A Subramanian. T hermoelectric Materials , Phenomena , and Applications : A Bird ' s Eye View. 31(March), 2006.

[45] J. L. T. Waugh and G. Dolling. Crystal dynamics of gallium arsenide. *Phys. Rev.*, 132:2410–2412, Dec 1963. doi: 10.1103/PhysRev.132.2410. URL `http://link.aps.org/doi/10.1103/PhysRev.132.2410`.

[46] Bartlomiej Wiendlocha. Localization and magnetism of the resonant impurity states in Ti doped PbTe. *Appl. Phys. Lett.*, 105(13):133901, 2014. ISSN 0003-6951. doi: 10.1063/1.4896856. URL `http://scitation.aip.org/content/aip/journal/apl/105/13/10.1063/1.4896856`.

[47] Wikipedia. Muybridge's *The Horse in Motion*:. `http://en.wikipedia.org/wiki/Eadweard_Muybridge#mediaviewer/File:The_Horse_in_Motion.jpg`.

[48] Ellen J. Yoffa. Screening of hot-carrier relaxation in highly photoexcited semiconductors. *Phys. Rev. B*, 23(4):1909–1919, 1981. ISSN 01631829. doi: 10.1103/PhysRevB.23.1909.

[49] I. I. Zasavitskii, E. A. de Andrada e Silva, E. Abramof, and P. J. McCann. Optical deformation potentials for pbse and pbte. *Phys. Rev. B*, 70:115302, Sep 2004. doi: 10.1103/PhysRevB.70.115302. URL `http://link.aps.org/doi/10.1103/PhysRevB.70.115302`.